THESIS FOR THE DEGREE OF LICENTIATE OF ENGINEERING

THz Ultra-wideband Passive Devices: Design, Simulation and Characterization

Cristian Daniel López

Department of Space, Earth and Environment

CHALMERS UNIVERSITY OF TECHNOLOGY

Gothenburg, Sweden 2021

THz Ultra-wideband Passive Devices:
Design, Simulation and Characterization
Cristian Daniel López

© Cristian Daniel López, 2021.

Department of Space, Earth and Environment
Chalmers University of Technology
SE-412 96 Gothenburg
Sweden
Telephone + 46 (0)31-772 1000

Cover:
Top Left: SEM image of the Substrateless Finline 211-375 GHz.
Top Right: Waveguide Chain for cryogenic measurements mounted inside a close-cycle cryostat.
Bottom Left: Electromagnetic simulation of 90° step-twist 140-220 GHz. Insert. Fabricated 90° step-twist.
Bottom Right: Fabricated superconducting slotline to microstrip transition 211-375 GHz.

Printed in Sweden by Chalmers Reproservice
Gothenburg, Sweden 2021

THz Ultra-wideband Passive Devices:
Design, Simulation and Characterization
CRISTIAN DANIEL LÓPEZ

Group for Advanced Receiver Development - GARD
Department of Space, Earth, and Environment
Chalmers University of Technology

Abstract

The last decades have seen an increasing interest in the THz research field, leading to a substantial improvement in technology and the emergence of new applications. In particular, the research on radio astronomy instrumentation has pushed millimeter and sub-millimeter technology boundaries and redefined state of the art. Nonetheless, the requirements set for the next generation of radio astronomy receivers will demand remarkable technological development, especially in terms of RF and IF bandwidth. Addressing this need, the present licentiate thesis focuses on the design, simulation and characterization of ultra-wideband THz passive devices for the next generation of radio astronomy receivers.

As THz receivers mixers are implemented with thin-film technology, waveguide to substrate transitions have a fundamental role in the performance and bandwidth of such systems. The critical requirements for these transitions are a proper impedance matching and the minimization of insertion loss. In this thesis, a waveguide to slotline superconducting transition based on substrateless finlines is proposed. The transition was designed for prospective broadband SIS mixer design in the frequency range 211-375 GHz. The experimental verification at cryogenic temperatures shows a remarkable fractional bandwidth of 55%.

Although this transition represents a substantial improvement over existing designs, it is important to note that it transforms a waveguide propagation mode into slotline mode. For the majority of modern SIS mixers, microstrip line topology is the most suitable. Hence, the ongoing development is focused on broadband slotline to microstrip transitions. In this work, a slotline to microstrip transition based on Marchand Balun is designed, simulated and fabricated. The electromagnetic simulations showed promising results, and the cryogenic characterization at 4K is ongoing.

For most modern polarization-sensitive THz receivers, 90° waveguide twists are essential interconnection parts. Since compactness and low insertion loss are critical requirements, single step-twists have emerged as an attractive solution. In this work, a novel compact wideband 90-degree twist for the 140-220 GHz band is presented. Furthermore, the proposed twist has a performance tolerant to small geometry variation, and hence it is especially suited for fabrication by direct milling. The experimental verification shows 44% fractional bandwidth with return loss better than 20 dB over most of the band.

Keywords: Compact waveguide twist, Substrateless Finline, Broadband Waveguide to Substrate Transition, Superconducting Transition, Marchand Baluns.

List of Publications

Appended Papers

Paper A: LÓPEZ, C., et al. Design and Implementation of a Compact 90° Waveguide Twist with Machining Tolerant Layout. *IEEE Microwave and Wireless Components Letters*, 2020, vol. 30, no 8, p. 741-744.

Paper B: LÓPEZ, C., et al. Waveguide-to-Substrate Transition Based on Unilateral Substrateless Finline Structure: Design, Fabrication, and Characterization. *IEEE Transactions on Terahertz Science and Technology*, 2020, vol. 10, no 6, p. 668-676.

Other Papers

[I] LÓPEZ, C., et al. Surface modification of polytetrafluoroethylene thin films by non-coherent UV light and water treatment for electrowetting applications. *Progress in Organic Coatings*, 2020, vol. 149, p. 105593.

[II] LÓPEZ, C., et al. Design, Fabrication and Characterization of Waveguide to Substrate Transition Based on Unilateral Substrateless Finline Structures. *Proc. 31th Int. Symp. Space Terahertz Technol.* 2020.

[III] LÓPEZ, C., et al. Broadband waveguide-to-substrate transition using a unilateral etched finline structure. *Proc. 30th Int. Symp. Space Terahertz Technol.* 2019. p. 47-48.

[IV] Pavolotsky, A., López, C. D., Tidekrans, I. V., Meledin, D., Desmaris, V., & Belitsky, V. Specific capacitance of Nb/Al-AlN/Nb superconducting tunnel junctions. *Proc. 30th Int. Symp. Space Terahertz Technol.* 2019. p. 92-94.

[V] LÓPEZ, C., et al. Design and Implementation of a Broadband and Compact 90-degree Waveguide Twist with Simplified Layout. *Proc. 30th Int. Symp. Space Terahertz Technol.* 2019. p. 42-43.

[VI] Gouda, Ahmed, López, C. D., Desmaris, V., Meledin, D., Pavolotskiy, A., & Belitsky, V. Millimeter-Wave Wideband Waveguide Power Divider with Improved Isolation between Output Ports. **To be publised in**: *IEEE Transactions on Terahertz Science and Technology*, 2021.

Acknowledgments

I would like to thank Prof. Victor Belitsky for the opportunity to pursue my PhD studies at the Group for Advanced Receiver Development where I have grown both professionally and personally. My special thanks to my main supervisor Prof. Vincent Desmaris for his teachings and his advice. I would like to thank Dr. Denis Meledin and Dr. Alexey Pavolotsky for sharing their wide knowledge and for their help and motivation. Furthermore, my sincere thanks to my colleagues and friends at GARD who are always ready to help me.

Deseo dedicar esta tesis a Marcela, mi esposa. Ella ha recorrido este largo y difícil camino siempre a mi lado. Esta tesis también es suya. Además, deseo agradecer a mis padres, que siguen apoyandome a la distancia, y a mi hermano, del que siempre estaré orgulloso. Por ultimo, agradecer a Joaquín por ayudarme a corregir este manuscrito y por su amistad.

List of Abbreviations

ALMA	Atacama Large Millimeter/Submillimeter Array
APEX	Atacama Pathfinder Experiment
BCS	Bardeen, Cooper and Schrieffer
CPW	Coplanar Waveguide
IV	Current Voltage
DC	Direct Current
DSB	Double Sideband
EHT	Event Horizon Telescope
GHz	Gigahertz
Au	Gold
HFSS	High Frequency Structure Simulator
HEB	Hot Electron Bolometer
IF	Intermediate Frequency
LO	Local Oscillator
LNA	Low Noise Amplifier
Nb	Niobium
NOEMA	Northern Extended Millimeter Array
OMT	Orthomode Transducer
RF	Radio Frequency
SEM	Scanning Electron Microscope
Si	Silicon
SiO2	Silicon Dioxide
SIS	Superconductor Isolator Superconductor
THz	Terahertz
TRL	Thru Reflect Line
TE	Transverse Electric mode
UV	Ultraviolet
VLBI	Very Long Baseline Interferometry

Table of Contents

Chapter 1 - Introduction

The human eyes perceive a small fraction of the electromagnetic spectrum that is commonly referred as visible light. Nevertheless, the electromagnetic spectrum extends far beyond the optical region, and it is traditionally divided from low to high frequency in: radio waves, microwaves, THz, infrared, visible light, UV, and X rays, as depicted in Figure 1.1. Among these spectral regions, the THz range, which falls between 100 GHz (3 mm) and 10 THz (3 0μm), has recently drawn increasing attention in the scientific community. The interest in this particular frequency range is motivated by its numerous applications in fundamental and applied science, e.g. bio- and medical science [2], material science [3], and radio astronomy [4]. Moreover, the continuous advancement in generation and measurement techniques at this frequency range is taking the THz wireless communications systems one step closer to reality [5]. These advancements have been led by the research on radio astronomy instrumentation which has continuously pushed the technological boundaries and redefined the state of the art technology at THz frequencies [6-8].

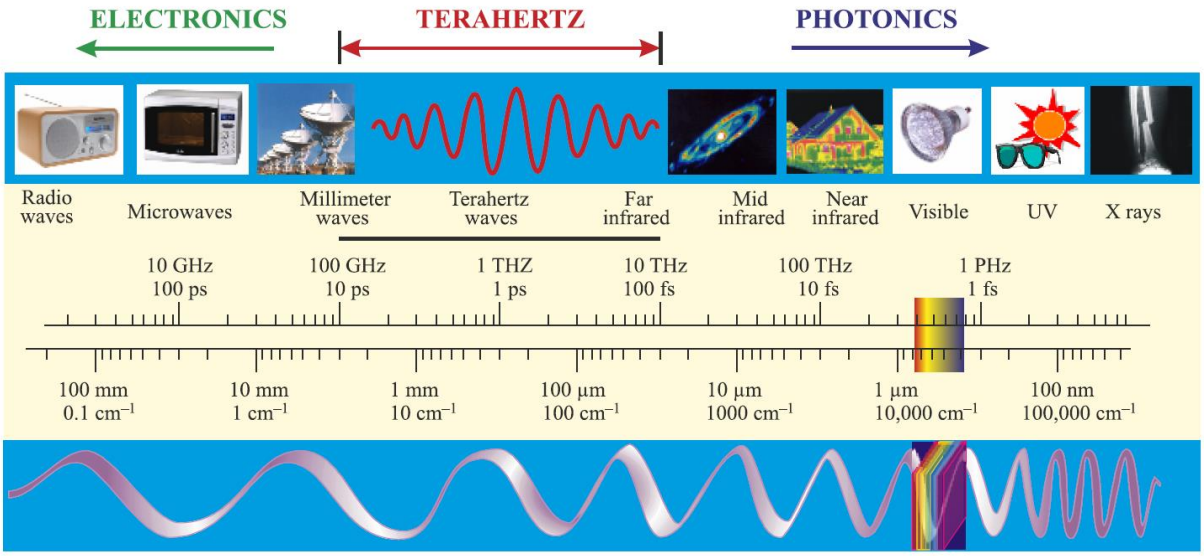

Figure 1.1. *Illustration of the electromagnetic spectrum divisions and frequency ranges. Reproduced from [1].*

For radio astronomy researchers, the study of this section of the electromagnetic spectrum is especially relevant since half of the luminosity of the Universe, and 98% of the emitted photon from the Big Bang corresponds to THz radiation [9]. The observation of the cosmos in the THz region holds the key for answering fundamental questions, ranging from the formation of our Solar System to the existence of life in other planets [4]. Answering these questions has inspired worldwide efforts to develop and build radio telescopes to perform high-resolution observations at millimetre and submillimetre wavelengths. In the last decade, these observations have led to significant milestones for radio astronomy. For instance, the first picture of a supermassive black hole was taken by the Event Horizon Telescope (EHT) [10]. The EHT is a virtual interferometric

telescope that spans nearly the diameter of the Earth by combining multiple telescopes located around the globe, e.g. the Northern Extended Millimeter Array (NOEMA) [11], the Atacama Pathfinder Experiment (APEX) [12] and the Atacama Large Millimeter/Submillimeter Array (ALMA) [13]. In Figure 1.2, a small selection of recent radio astronomy observations is shown.

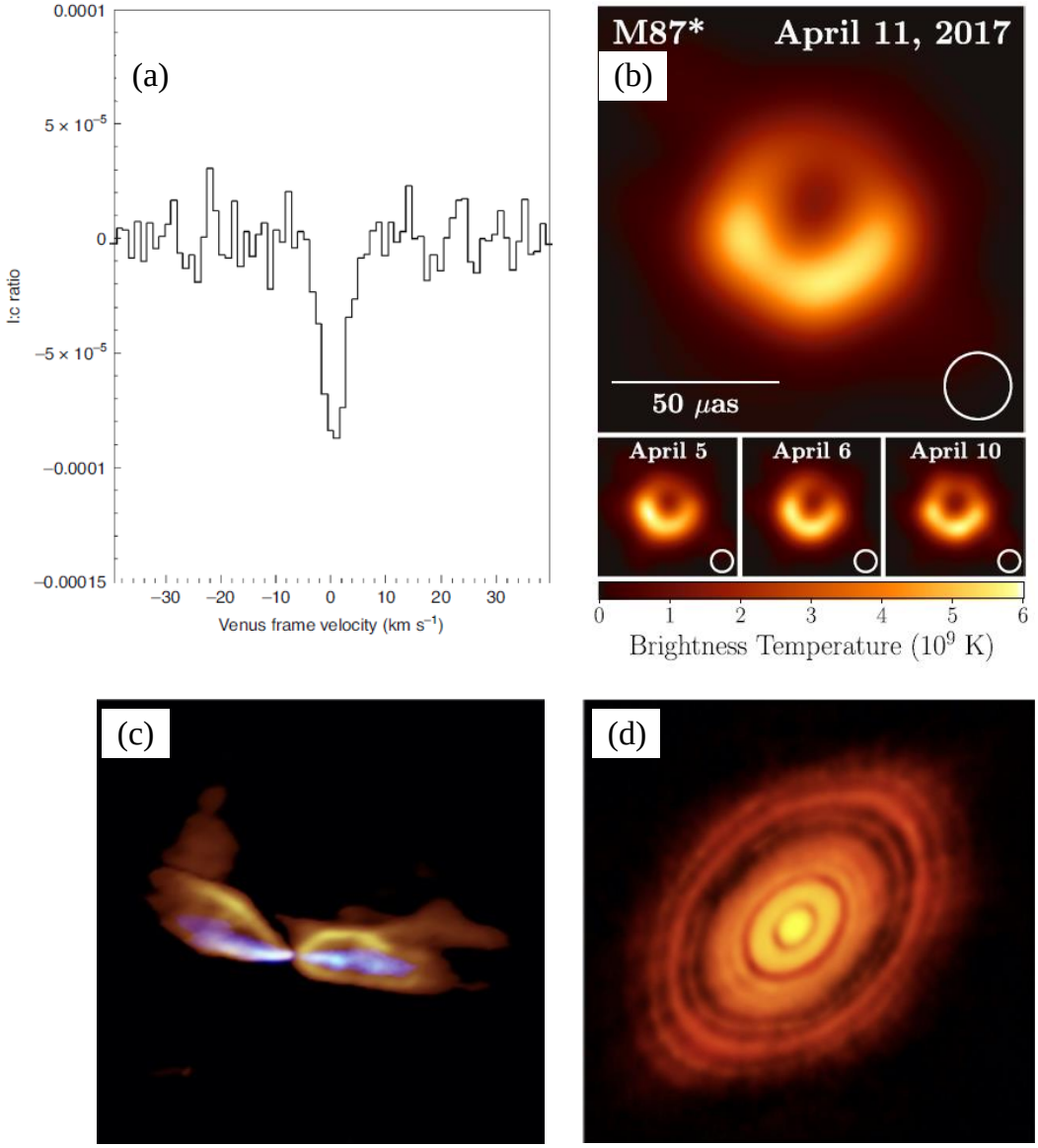

Figure 1.2. *Selection of recent radio astronomy observations. (a) Phosphine spectral signature from planet Venus obtained with ALMA. The presence of phosphine in the upper atmosphere of Venus could indicate the presence of life. However, this have not been confirmed. Extracted from [14]. (b) First picture of the supermassive black hole situated in the M87 galaxy obtained by the EHT [10]. (c) Image of a low velocity outflow from a protostar in Orion [15]. (d) Image of a protoplanetary disk [16].*

A large number of radio astronomy observations are performed employing state of the art heterodyne receivers with high spectral resolution. Although modern THz receivers have already achieved an outstanding performance [6,22,29], the science goals set for the next decades will demand remarkable technological development. The recommendations found in technological roadmaps such as the ALMA roadmap to 2030 [16], and VLBI 20-30: "a scientific roadmap for the next decade" [81], reflect the needs for the next generation of radio astronomy receivers. In particular, wider IF and RF bandwidths are of foremost importance for the future of radio astronomy. To secure a large instantaneous RF bandwidth, the present work proposes a number of ultra-wideband passive devices for the next generation of THz receivers. Nevertheless, it should be mentioned that these components are an attractive solution for a diverse range of applications, such as THz wireless communications [5] and bio- and medical science [2].

Thesis structure

The thesis consists of six chapters, two appendixes, a table of contents and bibliography. Chapter 1 and 2 provide a brief overview of the scientific and technological background behind this thesis. Chapter 3 details the design of a novel waveguide step twist for the frequency range 140-220 GHz. Meanwhile, Chapter 4 elaborates on the development of a novel type of finlines, the substrateless finlines. Moreover, Chapter 4 describes the design and the cryogenic measurements of a waveguide to substrate transition for the frequency range 211-375 GHz, which allows covering ALMA band 6 (211-275 GHz), and ALMA band 7 (275-375GHz) simultaneously. In Chapter 5, the work in progress on slotline to microstrip transitions based on Marchand Baluns is detailed. Finally, the concluding remarks and future outlook are presented in Chapter 6.

Chapter 2 - Scientific and Technological Background

Overview: This chapter provides scientific and technological background for the thesis. In section 2.1, the following fundamental concepts of radio astronomy receivers are explained: detector types, heterodyne detection fundamentals and the importance of the system noise temperature. These concepts set the foundations for the devices presented in this thesis, i.e. a compact single step 90° waveguide twist with a simplified layout, a waveguide to substrate transition based on the novel substrateless finlines, and a slotline to substrate transition based on Marchand Baluns. Section 2.2 details the most critical waveguide components for radio astronomy receivers. Among those, the 90° waveguide twists found in the literature are analyzed. This analysis allows us to define the motivation and background for the device presented in [Paper A]. Furthermore, Section 2.3 elaborates on the advantages and disadvantages of the existing waveguide to substrate transitions and the motivations behind the design presented in [Paper B]. Finally, section 2.4 explores the different slotline to microstrip transitions found in the literature and justifies the need for the ongoing research effort on ultrawideband Marchand Balun transitions.

Section 2.1 - Radio astronomy Detectors

The radio astronomy receivers are intended to detect extremely weak signals that can easily be outpowered by noise. The noise affecting the receiver might come from external and internal sources. However, in many cases, the ultimate noise performance of the receiver is limited by the noise produced in the detector itself. Therefore, the detector noise must be minimized. This requirement is critical for the receiver performance since the sensitivity of the radiotelescope is intrinsically related with the noise temperature by the radiometer equation [17]:

$$S \propto \frac{T_{SYS}}{\sqrt{\tau_{int}\, B}} \tag{2.1}$$

where S is the sensitivity, i.e. the minimum change in the input signal that the system can detect. Meanwhile, τ_{int} is the integration time, and B and T_{SYS} are the bandwidth and the noise temperature of the system, respectively. It is essential to mention that T_{SYS} is defined for the entire system and includes the contributions of the receiver, antenna, atmosphere, ground and source. From equation 2.1, it can be seen that the system noise temperature is linearly related to the sensitivity. In contrast, the dependence with the integration time is the inverse of the square root. These relations indicate that reducing the system noise temperature is the most efficient option to increase the sensitivity.

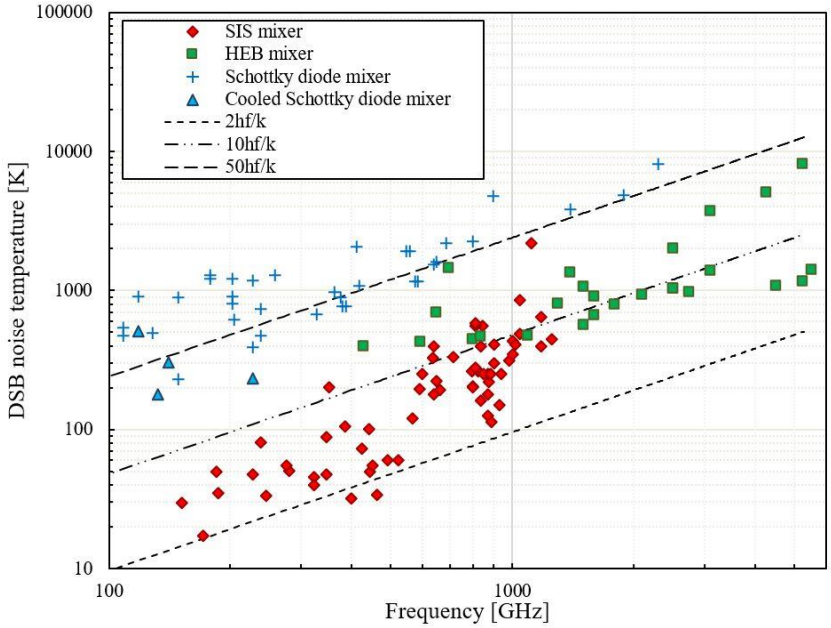

Figure 2.1. *The existing mixers technologies are compared based on their DSB noise and the frequency of operation. Extracted from [18].*

The radio astronomy receiver's low noise and high-frequency operation requirements have inspired the development of three leading technologies with their advantages and disadvantages. In Figure 2.1, the existing mixer technologies are organized according to their DSB noise temperature and frequency of operation.

Schottky diode mixers emerge as an attractive solution due to their large IF bandwidth and wide temperature range of operation [19]. However, the demand for a considerable LO power (~mW) and the comparably high noise temperature makes them less attractive for applications that require the ultimate sensitivity, e.g. radio astronomy instrumentation.

Superconducting hot electron bolometers (HEB) provided the best noise performance for frequencies above 1 THz. Their principle of operation relies on heating with microwave radiation an ultrathin superconducting film. As the heating process does not depend on the frequency of the incident radiation, HEB can provide unlimited RF bandwidth. Nevertheless, the thermal response sets a limit in the IF bandwidth of HEB mixers. Even though substantial progress towards larger IF bandwidths has been made in recent years [8,77], the IF bandwidth remains the main challenge for HEB mixers.

Superconductor-insulator-superconductor (SIS) mixers present an outstanding noise performance in the frequency range from 100 GHz to 1.2 THz. In particular, when they operate in quantum mode it is possible to approach the theoretical quantum noise limit hf/2k, as it was demonstrated in [6,20]. Since the components presented in this work are meant for prospective SIS mixer design, the basic working principles behind this mixer type will be detailed. The working principle behind SIS mixers lies in the photon assisted quasiparticle tunnelling through a superconductor-insulator-superconductor SIS tunnel junction. Figure 2.2a illustrates the energy level diagram of a SIS structure. From the Figure, it can be seen that a gap exists between the filled states (shaded) and

the empty states. Ideally, at T=0K, the filled states are fully occupied by paired electrons denominated "Cooper pairs". Meanwhile, at $0<T<T_{critical,}$ a fraction of superconducting pairs breaks into single electrons, and they are exited into quasiparticle energy state. When the SIS is biased to a voltage level of $Vb \geq 2\Delta/e$, where "Δ" is the superconductor bandgap, and "e" is the electron's charge, the filled states on the left approach the level of the unfiled band on the right. Therefore, the cooper pairs can be broken, and the resulting quasiparticles can tunnel through the insulating layer. In the presence of a photon source with energy hf, the tunnelling can occur at a lower bias voltage, i.e. hf/e. This phenomenon could be used for developing heterodyne mixers. It is important to note that the tunnelling of Cooper pairs, known as the Josephson Effect, is an undesirable effect in SIS mixers since it increases the overall noise. Thus, a steady magnetic field is employed to suppress cooper pair tunnelling. Another interesting feature of SIS mixers is that in contrast to conventional mixers, it is possible to have conversion gain as described in [76].

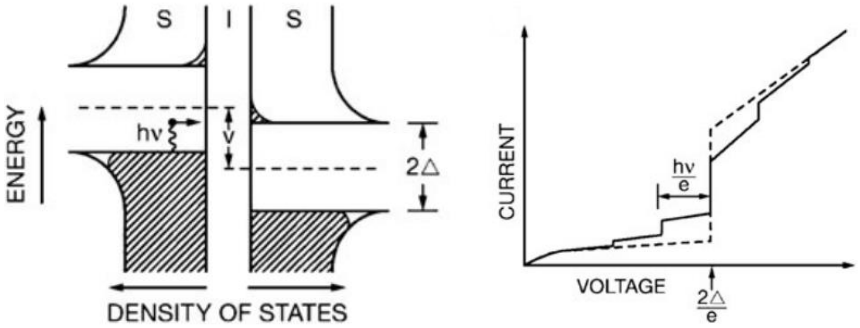

Figure 2.2. *SIS principle of operation. Extracted from* [21]. *(a) Energy bands of a biased superconducting-insulating-superconducting (SIS) structure. The copper pair is broken by the incoming photon which allows the quasiparticle to tunnel through the insulator. (b) IV curve of the SIS junction. The dashed line corresponds to the unpumped SIS, i.e. when no local oscillator (LO) power is applied. Meanwhile, the solid line shows the behavior with the applied LO power.*

The SIS junction's structure sets limits for the IF bandwidth and the operational frequency since the IF bandwidth is limited by the geometrical capacitance of the junction. Moreover, the IF bandwidth is further limited by the tuning circuitry capacitance.

The choice of a mixer technology will depend on the characteristics of the radiotelescope, frequency of operation and noise requirements. Moreover, the receiver detection could be coherent or incoherent. In contrast to incoherent detection, heterodyne (coherent) receivers preserve the phase information of the incoming radiation. The following section elaborates on the key concepts of heterodyne detection.

Concepts of Heterodyne Detection

A frequency mixer is essentially an analogue multiplication of two signals with different frequencies denominated Local Oscillator (LO) and Radio Frequency (RF). The LO is generated in a reference source, while the RF signal presents the information of interest. The mixing between the LO and the RF produces a signal called Intermediate Frequency (IF) that fully preserves the phase and amplitude of the RF information. The IF frequency is higher or lower than the RF depending on whether the process is up-conversion or down-conversion. While up-conversion is typically employed in transmitters, the down-conversion process is found in receivers[1].

The mixer element's nonlinear nature produces a large variety of harmonics and undesired signals that must be filtered out at the output. The following power series function describes a classical regime mixer response:

$$I(t) = a_0 + a_1 V(t) + a_2 V(t)^2 + a_3 V(t)^3 + \cdots a_n V(t)^n \tag{2.2}$$

Where $I(t)$ is the time dependent current at the mixer output. When LO and RF are applied , $V(t)$ is defined as:

$$V(t) = V_{LO} \cos(2\pi f_{LO} t) + V_{RF} \cos(2\pi f_{RF} t) \tag{2.3}$$

Therefore, the mixer will generate at its output a large number of frequency components based on the addition, subtraction and multiplication of the original f_{LO} and f_{RF}. However, the frequency components that are interesting for the conversion process are:

$$I(t) \propto \mathrm{K} \cos(2\pi f_{LO} t) \cos(2\pi f_{RF} t) \tag{2.4}$$

$$I(t) \propto \frac{\mathrm{K}}{2} [\cos 2\pi (f_{RF} + f_{LO}) t + \cos 2\pi (f_{RF} - f_{LO}) t] \tag{2.5}$$

$$f_{IF} = f_{RF} \pm f_{LO} \tag{2.6}$$

The intermediate frequency can be filtered from the rest of the undesirable frequency components.

Many radio astronomy receivers make use of the down-conversion process to detect and process the high frequency signals that come from celestial bodies, e.g. [6,22,23,29]. In Figure 2.3, the simplified block diagram for a heterodyne radio astronomy receiver is shown. The bandpass response is provided by the interconnection components located between the antenna and the mixing element, i.e. horn, orthomode transducer (OMT), and waveguide to substrate transition.

It is essential to note that radio astronomy receivers operating below ~100 GHz incorporate a RF low noise amplifier (LNA) as the first stage, e.g. ALMA band 2 receiver [24]. Even though LNA technology is progressing towards frequencies above ~100 GHz, e.g. [25,26], RF LNAs are not employed in high frequency receivers since the noise of such devices so far is too large compared to the extremely sensitive SIS mixer. Therefore, the inclusion of an RF LNA would deteriorate the

[1] Part of this section follows the book by David Pozar "Microwave Engineering"

noise performance of the system. This aspect will be further discussed in the next section, where the system noise temperature is presented.

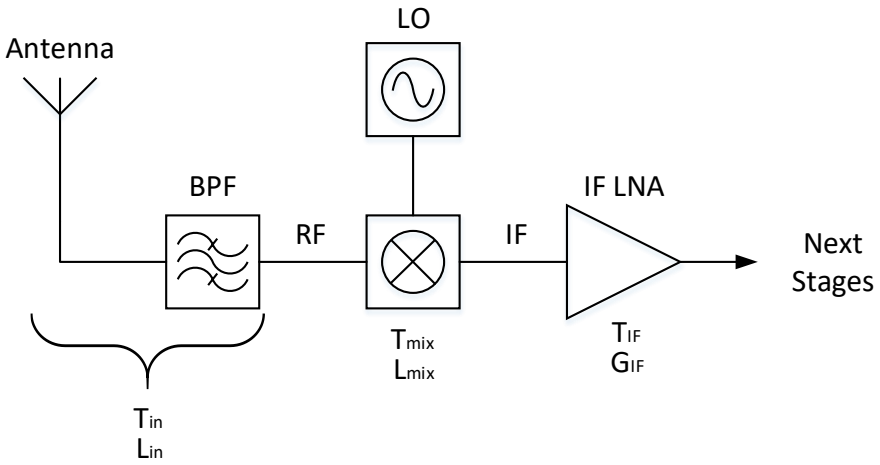

Figure 2.3. *Simplified block diagram for heterodyne receivers for radio astronomy applications.*

System Noise Temperature

Since the temperature of a system is inherently connected to the generated noise power, the measurement of equivalent noise temperature provides a figure of merit to evaluate the receiver's performance. The equivalent noise temperature could be defined as the absolute temperature of an equivalent resistor that would generate the same noise as the component [27]. This definition could be better understood with the following example. In Figure 2.4a, a noisy amplifier with bandwidth B and gain G is depicted. The amplifier is perfectly matched to a source and load resistors which are noiseless. If the absolute temperature of the input resistor is 0 K, the input noise power would be 0, thus, the output noise power would be the noise generated by the amplifier itself. As depicted in Figure 2.4.b, it is possible to obtain the same noise output power if the amplifier is assumed noiseless and the resistor is at a temperature T_e:

$$N_0 = GkT_eB \tag{2.7}$$

where k is the Boltzmann's constant and B the bandwidth of the system. Therefore, T_e is the equivalent noise temperature of the amplifier. Moreover, the T_e of a passive device is tightly connected to its losses [27]:

$$Te = (L-1)T \tag{2.8}$$

Where T is the temperature of the passive device, and L are the losses which are defined as the loss of signal power resulting from the insertion of the passive device in the transmission path. Therefore, reducing the system noise might be achieved by minimizing their components' losses and decreasing operation temperature. Both strategies are implemented in radio astronomy receivers where the losses are carefully optimized, and the system is generally cooled down to

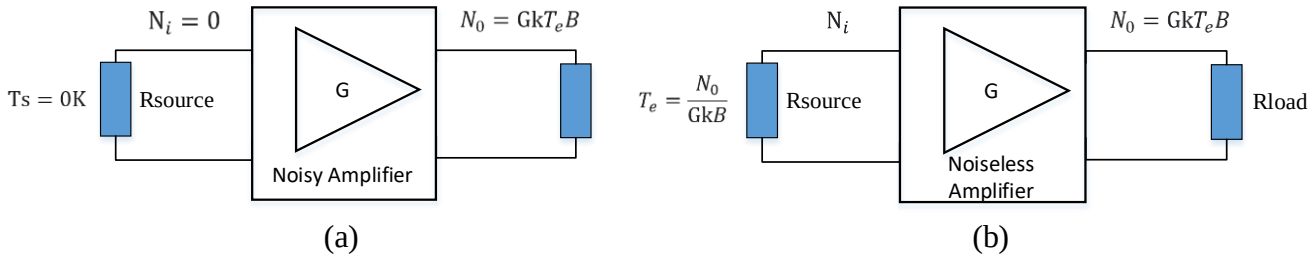

Figure 2.4. *Definition of equivalent noise temperature of a noisy amplifier. (a) Noisy amplifier (b) The output noise power is identical if the amplifier is noiseless and the source resistance is at T_e temperature.*

cryogenic temperature to reduce the thermal noise. It is important to note that the cryogenic operation is not only grounded by noise reduction but also required for the superconducting detectors functioning.

The system noise temperature for the system shown in Figure 2.3 is defined by cascading the individual contribution of each component as follows:

$$T_{sys} = T_{in} + L_{in}\left[T_{mix} + L_{mix}\left(T_{IF} + \frac{T_{next\_stage}}{G_{IF}}\right)\right] \tag{2.9}$$

From the equation, it becomes clear that the first stages significantly impact the overall system noise temperature. In SIS mixer radio astronomy receivers operating beyond ~100 GHz, LNAs are not useful since the noise added by this component as first stage amplifier would dominate the overall system noise temperature. Thus, the SIS mixer is employed as the first stage of the system. It is important to note that SIS mixers can achieve conversion gain [76], and therefore, the term L_{mix} could be replaced by $1/G_{mix}$ which will help to reduce the overall T_{sys}. Nevertheless, SIS mixers with high conversion gain are not frequently employed due to potential oscillations and difficulties in the design for wideband operation.

T_{in} represents the noise of the antenna, optics and all the components located before the mixer stage, e.g. waveguide to substrate transitions and, in polarization sensitive receivers [6,29,78], OMT and waveguide twist. Moreover, the losses of such components are represented by L_{in}. From equation 2.9, it is seen that the input losses should be minimized to reduce their impact on the overall system noise temperature. Therefore, the minimization of losses was one of the main requirements for the design of the devices presented in this thesis, i.e. waveguide to substrate transition and waveguide twist.

Section 2.2 - Waveguide Components

Radio astronomy receivers make use of waveguide components to transport the RF and LO signals. Among the different components, the most critical for the receiver performance are the feed horns and the orthomode transducers (OMTs). The feed horn is used to couple the incoming electromagnetic radiation into the waveguide system. Meanwhile, the OMT, which is connected at the output of the feed horn, is used for polarization discrimination [28]. OMTs are widely employed in modern polarization-sensitive receivers such as [6,29] to detect the incoming signal's polarization. Since the outputs of the OMTs are generally orthogonal to each other, the E field of one of the output waveguides often needs to be rotated 90° to facilitate the integration of the two signals chains into a single receiver system, as depicted in Figure 2.5. Therefore, waveguide twists have become a crucial component for receivers with polarization discrimination. This waveguide component should achieve the E-field rotation with minimum losses since it is located in one RF path before the mixer. Thus, the twist's overall losses will directly impact the noise performance of the receiver and the symmetry of both polarization paths. Moreover, since the minimization of the losses is closely tied to the shortening of the RF path, the compactness of waveguide twists is also an essential requirement. It is important to highlight that compact and low loss waveguide twists are not limited to radio astronomy receivers, but they are frequently applied to many mm-wave and sub-mm systems too. For instance, highly integrated waveguide components are important for satellite systems where space and RF power are extremely limited [30].

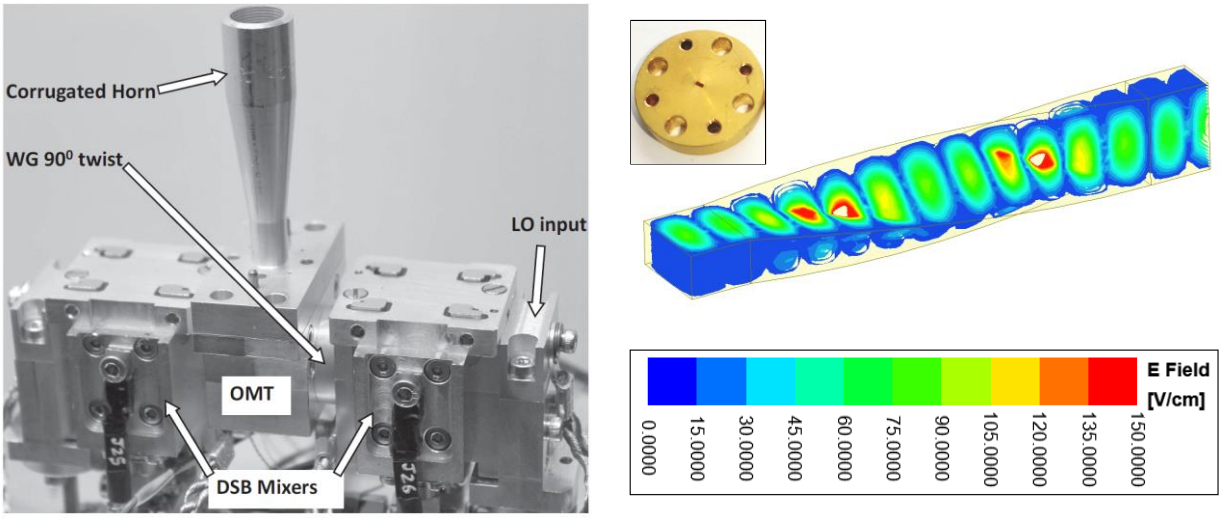

(a) (b)

Figure 2.5*. Continuous rotation twists (a) Example of 90° continuous twist employed after the OMT in ALMA band 5 preproduction cartridge [6] (b) E-field magnitude simulation of a continuous twist. It is appreciated how the E-field of the rectangular waveguide main mode is gradually rotated along the continuous twist. Top: image of continuous 90° waveguide twist employed in [6].*

90° Waveguide Twists

A great variety of 90° waveguide twists have been extensively studied in recent years to achieve compactness, low insertion loss and minimum reflections [31-41]. These designs tend to differentiate from commercially available solutions where continuous rotation twist are frequently

employed. Continuous twist relies on the gradual rotation of the E-field inside a twisted rectangular waveguide, as shown by Figure 2.5b. The gradual rotation guarantees broadband operation with minimum reflections. However, continuous twists require a length of several guided wavelengths, which makes them incompatible with highly integrated waveguide systems. Moreover, the electroforming process employed for its fabrication is costly and takes a significant amount of time.

An alternative solution was explored in the designs presented in [32-34], which are based on multi-step twists. These twists are formed by a series of waveguide sections that are gradually rotated until the full E-field rotation is achieved. Although this solution is less bulky than continuous twist, its fabrication is rather complicated. Furthermore, the overall performance of the multi-step twists depends on the fabrication and mounting tolerances of each section. Therefore, these twists are especially challenging to implement at higher frequencies where mounting tolerances are more critical.

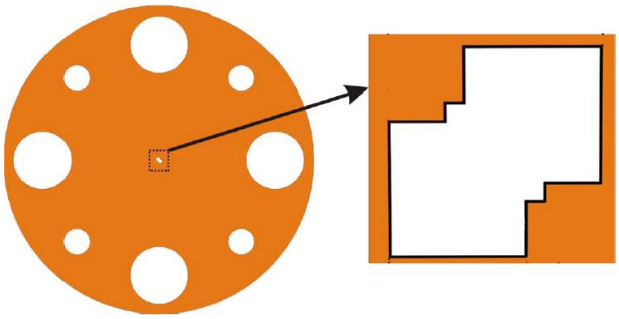

***Figure 2.6**. Single step twist with a corner cut layout proposed in [40] and fabricated by micromachining.*

The 90° single-step twists constitute the most compact solution. In this approach, a single waveguide section is inserted with an angle of 45°, which allows the E-field to rotate. As explained in [38], the discontinuities introduced by this waveguide section are mutually cancelled if the thickness is approximately one quarter guided wavelength ($\lambda_g/4$). Furthermore, the bandwidth and performance are related to the shape of the cross-section of the step twist. As a consequence, various shapes have been extensively studied [35, 38, 39, 41]. In particular, the corner cut shapes with multiple sharp corners have been widely adopted since they tend to maximize the bandwidth of the twist. Figure 2.6 illustrates a single step twist with sharp corners proposed in [40]. The sharp corners are rather challenging to fabricate with simple techniques as direct milling, especially at higher frequencies. This has led to alternative fabrication methods, as presented in [40], where micromachining techniques are employed for producing a 90° step twist. Although micromachining allows to precisely define the cross-section shape, it is so far a rather complicated and expensive process. Furthermore, the alignment of the twist with the input and output waveguides is critical to avoid in-band resonances, as demonstrated in [Paper A].

To address these problems, in this work, we demonstrate a novel compact wideband 90° twist with a performance less sensitive to geometry variations [Paper A].

Section 2.3 - Waveguide to Substrate Transitions

Thin-film technology is the main pillar for mixer fabrication in radio astronomy receivers, thus, waveguide to substrate transitions play a crucial role in the receiver performance. The main requirements for the waveguide to substrate transitions are a low insertion loss accompanied by proper impedance matching. In addition, a simple mounting process and the associated mounting tolerances are also essential requirements.

E-Probes

E-probes have been extensively employed from the origins of microwave technology to our days in a large number of applications. This enormous popularity responds to their ease of fabrication and versatility. Thanks to these characteristics, E-probes are among the most widely used waveguide to substrate transition for THz application. Moreover, the analysis of "one-side" microstrip probes impedance presented in [42] and [43] opened new possibilities for high-frequency broadband applications. In recent years, significant progress has been made toward wideband microstrip probes with fractional bandwidth reaching 50% [43]. In Figure 2.7, examples of E-probe radio astronomy mixers for different frequencies and detectors types are depicted.

Among the great variety of probe shapes found in the literature [45, 46, 47, 48], the radial probes are the most popular due to their convenient impedance range that can vary between 10 and 60 Ω

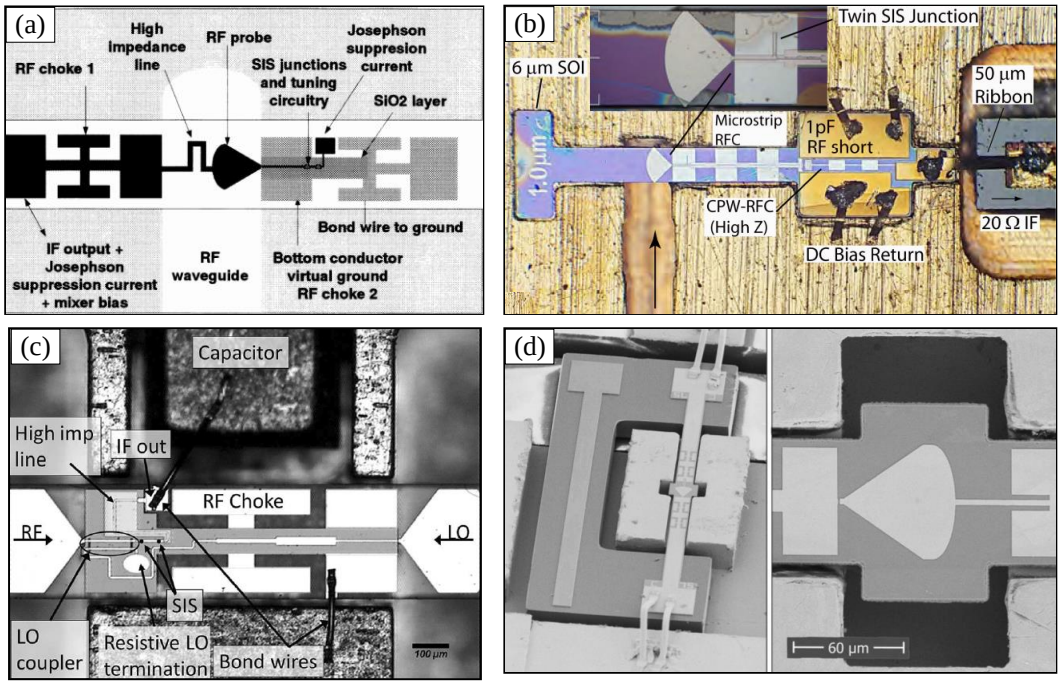

Figure 2.7. *Examples of E-probe radio astronomy mixers. (a) SIS mixer developed for APEX band 2 receiver covering 275-370 GHz [44]. (b) SIS mixer for 475 to 625 GHz [20]. (c) SIS mixer developed for ALMA band 5 receiver 163-211 GHz [45]. (d) NbN/GaN HEB mixer 1-1.5 THz [8].*

depending on the substrate and radius [43]. The pure real impedances can only be obtained by tuning out the impedance imaginary part. This cancellation is strongly dependent on the probe's position with respect to a waveguide backshort. The backshort is generally situated at $\lambda_g/4$ and constitutes the main limitation for the maximum bandwidth of E-probes. Thus, the mounting accuracy and machining tolerances become rather critical for the performance, especially at mm-wave and THz frequencies. In [43], a capacitive step is introduced in the input waveguide to increase the fractional bandwidth. Although this approach dramatically improves the probe's bandwidth, it does not solve the tolerance issues associated with E probes. Therefore, it becomes clear that there is a need for an alternative waveguide to substrate transition for the next generation of radio astronomy receivers.

Finlines

Since finlines structures were first proposed in [49], they have been used for a wide variety of applications, from microwave to the millimetre-wave range [50-53]. Finlines are waveguide to substrate transitions constitute by a pair of conductive fins over a dielectric substrate. It is important to remark that finline structures are meant for split block technology. In general, the conductive fins are positioned where the E-field magnitude is maximum for the fundamental TE_{10} rectangular waveguide mode, i.e. at the centre of the waveguide "a" dimension, as shown in Figure 2.8a. The positioning inside the rectangular waveguide gives finlines a considerable advantage with respect to other waveguide to substrate transitions, i.e. their tolerance to mounting and more straightforward block fabrication since a backshort is not needed.

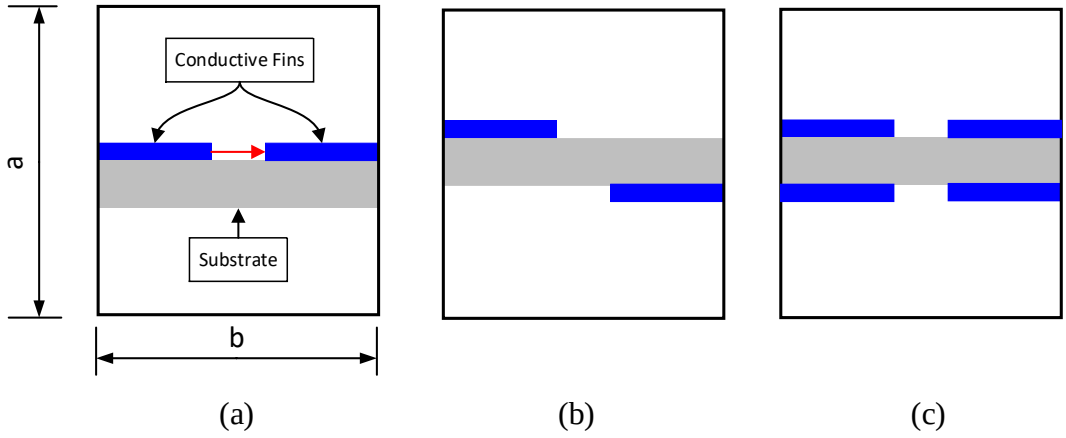

Figure 2.8. *Cross section of three commonly used finline configuration. (a) In the unilateral finline configuration the fins are located on only one side of the substrate. The red arrow illustrates the electric field excitation of the fin-gap (b) Antipodal finline configuration with separated fins by the substrate. (c) Bilateral Finline.*

Among the different existing configurations, the antipodal, unilateral and bilateral finlines are the most widely used. In antipodal finlines, the fins are separated by the substrate, as shown in Figure 2.8b. Antipodal finlines achieve lower impedance levels since the field is concentrated inside the substrate. Moreover, the antipodal layout allows a direct transition to microstrip. This advantage has been explored in [54], where an antipodal finline mixer was developed. However, the

performance of the antipodal configurations is sensitive to the alignment between the fins, especially at high frequencies where a few µm wide fin-gap is frequently employed. This problem is shared with the bilateral finline configuration since it presents a pair of fins on both sides of the dielectric slab, as depicted in Figure 2.8c. Furthermore, the bilateral arrangement generally presents significant losses due to higher field concentration inside the dielectric.

The unilateral layout is the simplest and probably the best suited for high-frequency applications since both metallizations are located on the same side of the dielectric slab, as illustrated by Figure 2.8a. This configuration eliminates the problems related to the fins' alignment but increases the overall impedance of the line since a large part of the electromagnetic field propagates outside the dielectric. The unilateral configuration has been applied for mixer design in [51]. In these designs, different techniques were employed to mitigate the main problem associated with finlines, i.e. the impedance matching between the waveguide and the substrate. The poor impedance matching degrades the performance of the transition and limits its operating bandwidth. In Figure 2.9, a

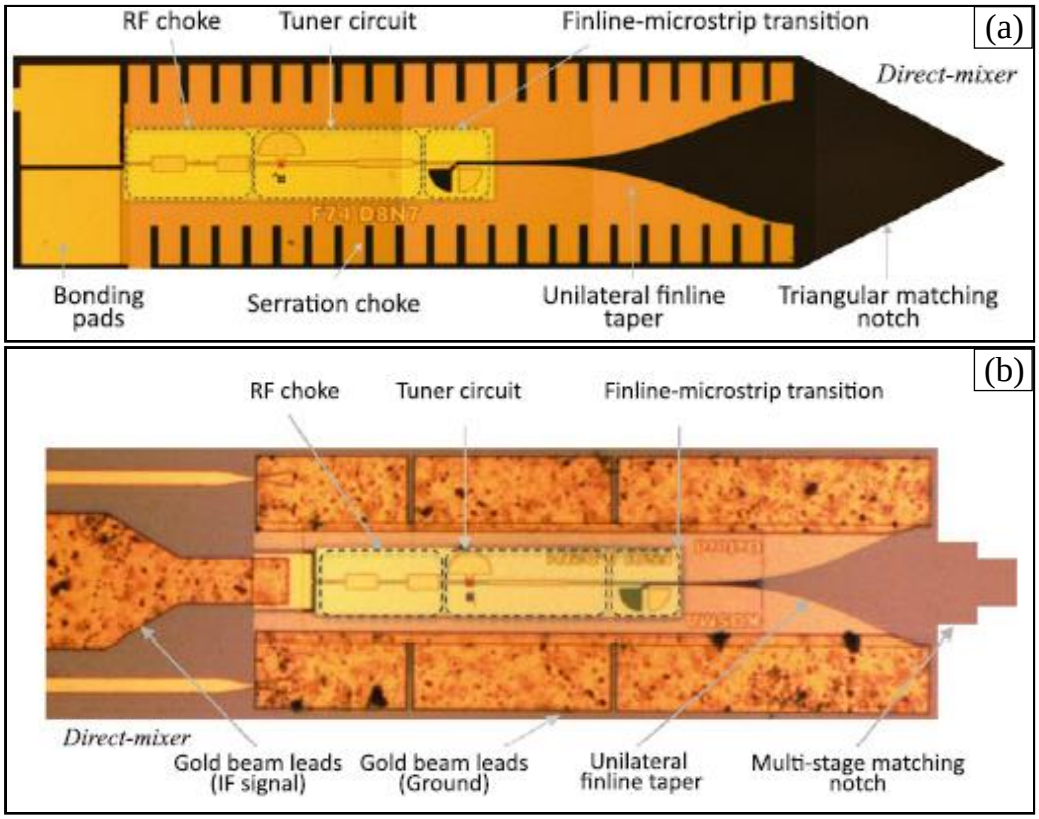

Figure 2.9. *Examples of unilateral finline 600-700 GHz radio astronomy mixers. Extracted from [55]. (a) SIS mixer fabricated over 60 µm quartz. The finline transition make use of a triangular notch in the quartz substrate to improve matching. In addition, serration chokes are employed to guard against the propagation of substrate mode. (b) SIS mixer fabricated over 15 µm Si substrate. Note the multi-stage silicon matching notch.*

variety of solutions for improving the matching are presented. These solutions are based on impedance transformers patterned on the substrate aiming to gradually load the waveguide and minimize the mismatch. Although these techniques partially solved the matching problem, they extend the substrate inside the waveguide, which increase the dielectric losses of the transition. An alternative solution is explored in this thesis [Paper B], where a new type of finline is presented, the Substrateless finline. In this finline configuration, the substrate confined by the fins is removed to improve the matching and reduce the dielectric losses.

Section 2.4 - Slotline to Microstrip transitions

Thin-film superconducting microstrips are fully compatible with the fabrication of the trilayer SIS structure. Furthermore, thin-film microstrips can reach impedances below 10 Ω, which is especially suitable for the SIS RF impedance matching circuit. Consequently, most modern SIS mixers rely on thin-film microstrip lines for on-substrate interconnections [45], [79]. On the other hand, finline structures can be easily coupled to slotlines as the main electromagnetic propagation mode is essentially identical. Nevertheless, fabricating slotlines with small characteristic impedance is rather challenging. Therefore, finline mixers usually employ an additional transition step from slotline to microstrip.

The main requirements for slotline to microstrip transitions are low insertion loss, high return loss, and chip area minimization. These requirements are challenging to accomplish due to the inherent impedance difference between slotlines and microstrips. While 40 Ω slotlines can be fabricated with thin-film technology, lower impedance values are non-practical as the slot dimension decrease to the μm range and below. On the other hand, it is rather difficult to achieved impedance values higher than 20 Ω with thin-film microstrips, where the dielectric layer thickness is comparable to the strip thickness. Therefore, the matching between slotlines and thin-film microstrip is highly complex. Through the years, a large number of different solutions have been proposed [55-59].

One of the classical solutions is the cross-junction transition [58], as depicted in Figure 2.10a. In these junctions, the microstrip is defined on one side of the dielectric, while the slotline is located on the opposite side. The transmission lines cross each other at a 90° angle and terminate in λ/4 stubs. These stubs are open and short circuit for the microstrip and the slotline, respectively. Therefore, the electromagnetic energy is transferred at the intersection from one transmission line into the other through the magnetic field. The energy transfer is maximized when the stubs are exactly λ/4 long. Hence, the cross-junction transition performance is limited by the stubs bandwidth. Radial stubs are frequently employed since they provide larger fractional bandwidth. However, the radial stubs dramatically increase the chip area together with the equivalent capacitance showed by the circuit at lower frequencies. This becomes especially problematic for SIS mixers where the IF bandwidth depends on a lower capacitance value.

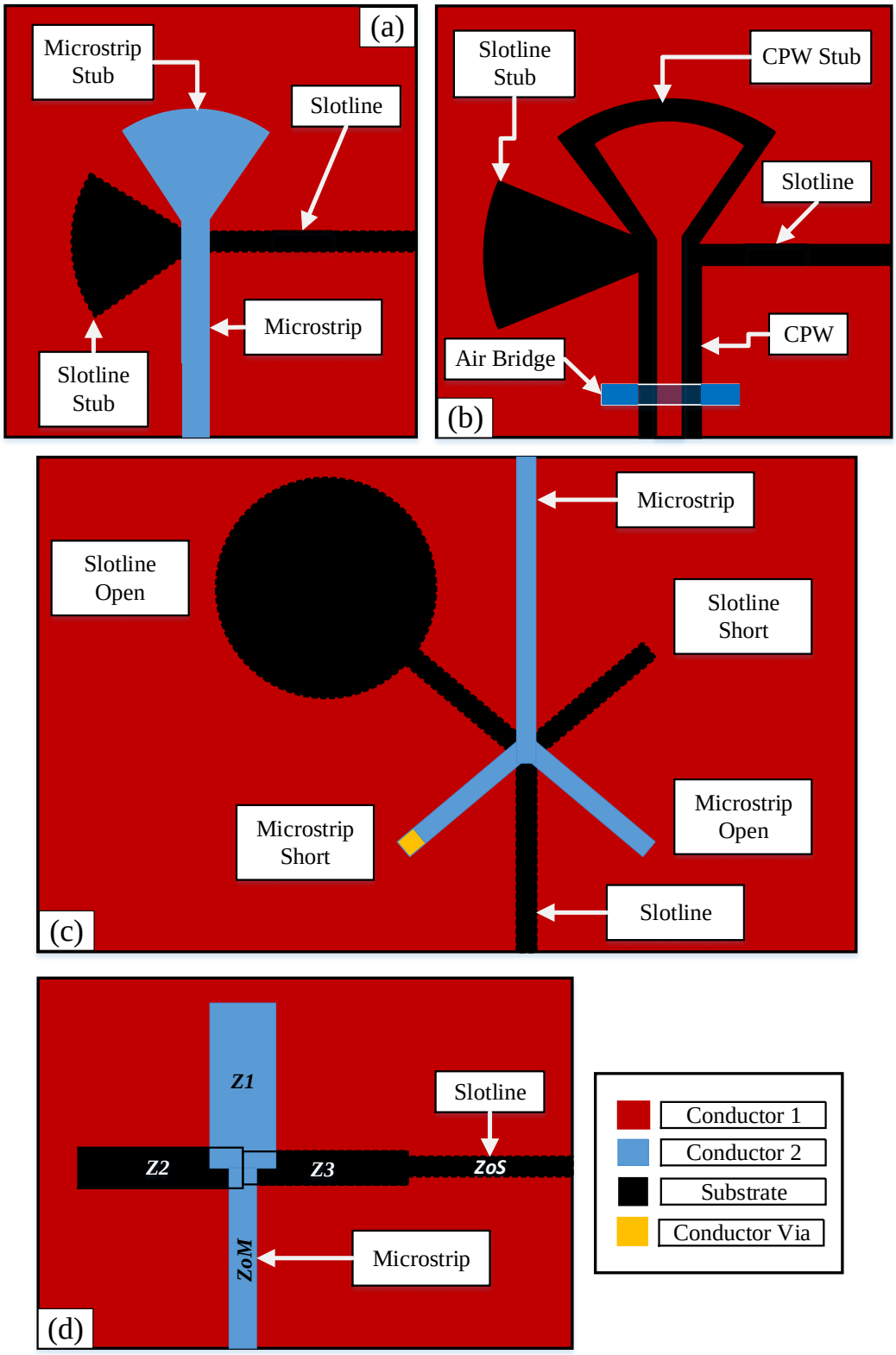

Figure 2.10. *Slotline to microstrip transitions. It is important to note that the dielectric layer located between the conductors is not shown in the images for clarity. (a) Cross-junction transition. (b) Indirect transition with CPW. (c) Double Y balun transition (d) Marchand balun transition.*

Double Y baluns emerge as an alternative solution to cross-junction transitions [59], as displayed in Figure 2.10c. The double Y balun employs short and opens terminations for both microstrip and slotlines to optimize energy transfer and improve the overall bandwidth of the transition. Nonetheless, the slotline open termination significantly increases the area on the chip, and it is a potential source of resonances due to energy radiation. Furthermore, the realization of the microstrip short makes the design and fabrication rather complex.

The inherent impedance difference of microstrips and slotlines could be overcome with indirect transitions, where an auxiliary transmission line is employed to facilitate the matching [55]. Among the different auxiliary lines, coplanar waveguides (CPW) are the most popular solution due to the wide range of impedances and field compatibility with slotline and microstrip, as illustrated by Figure 2.10b. Indirect transitions with CPW enhance the bandwidth of microstrip to slotline transitions. Nevertheless, the fabrication of such transition is rather complex due to the extra transition steps and the need for an air bridge to suppress parasitic CPW modes.

The Marchand balun transition arises as a promising solution due to its compactness and design flexibility [56]. The Marchand balun structures resemble the cross-junction transition. However, its bandwidth does not rely on single λ/4 stubs, but it combines different impedances to synthesize a particular response. For instance, a third-order Chebyshev passband response could be synthesized as depicted in Figure 2.10d. Furthermore, since this balun does not employ radial or circular stubs, the transition is highly compact. These characteristics make Marchand baluns an attractive solution for broadband low-loss microstrip to slotline transitions. In this work, the ongoing research towards a Marchand balun transition designed for future SIS mixer design and integration with substrateless finlines is presented in Chapter 5.

Chapter 3 - Wideband 90° Waveguide Twist with Simplified Layout for 140-220 GHz

In [Paper A], a novel compact wideband 90° twist was presented with a performance less sensitive to geometry variations than the existing corner cut designs, e.g. [35, 38, 39]. The higher geometric tolerance of the design allowed simple fabrication techniques as direct milling without compromising the overall bandwidth and the performance. The design layout presented in Figure 4.1 was intended for the 140-220 GHz band.

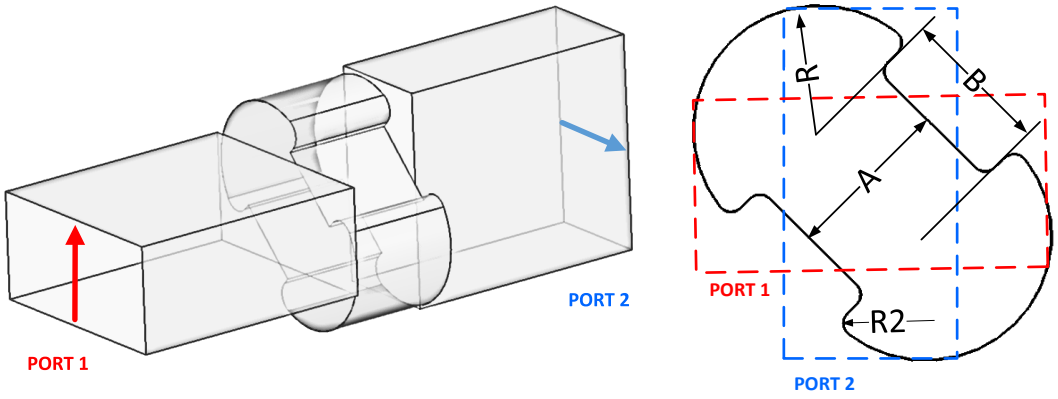

(a) (b)

Figure 3.1. *Waveguide twist presented in [Paper A]. (a) Waveguide twist layout. (b) Cross Section view and waveguide ports. Dimensions for WR-5.1 Band: R= 460µm, A= 600 µm, B= 500 µm and R2= 100 µm. The thickness of the step twist is 660 µm.*

Section 4.1 - Simulation of electromagnetic twist modes

The field rotation process can be better explained if the modes inside the twist cavity are studied. Figure 3.2 illustrates the electrical field distribution of the first, second and third modes of the twist cavity. As can be seen, the modes resemble TE_{10}, TE_{11}, and the antisymmetric TE_{10} modes in a rectangular waveguide, respectively. However, it is essential to highlight that the twist's second and third modes are evanescent for the input/output rectangular waveguides connected at port 1 and 2, i.e., they propagate only inside the twist cavity.

To further investigate the propagation modes of the twist, a series of simulations were performed. Figure 3.3 shows the simulated magnitude of S12 for two configurations: I) the twist as a standalone component and II) the twist connected to a standard rectangular waveguide in only one of its ports, as shown in the insert in Figure 3.3. In both configurations, the first three modes were simulated. For the first configuration, the cut-off frequencies were found to be 120 GHz, 211 GHz and 223 GHz. Note that the main mode for the standalone twist was not plotted since it propagates in the whole frequency band and may reduce the graph's clarity.

When the first configuration is compared with the second, a series of interesting conclusions can be drawn. In the first place, the second mode's cut off frequency is influenced by the rectangular waveguide connected to the twist. In contrast, the third mode cut off remains fixed, but a resonance appears at the same frequency, i.e., 223 GHz. This resonance is "mirrored" at the main mode, as seen in Figure 3.3. Therefore, the third mode will play a significant role in limiting the operational

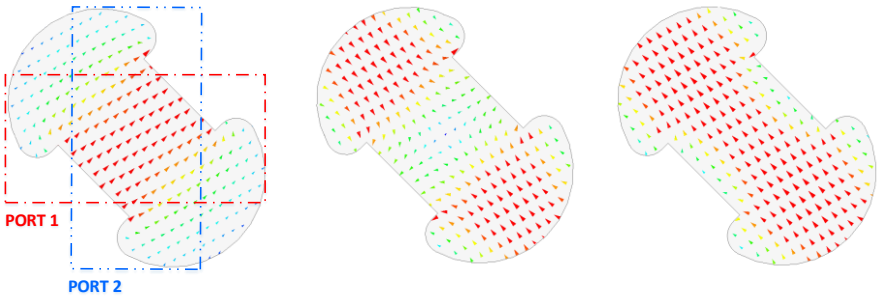

(a) (b) (c)

Figure 3.2. *Electrical field distribution comparison between Twist modes and standard rectangular waveguide WR 5.1. Twist modes: (a) Dominant Mode – Cut off Frequency 120 GHz. (b) Second Mode - Cut off Frequency 211 GHz.(c) Third Mode – Cut off Frequency 223 GHz.*

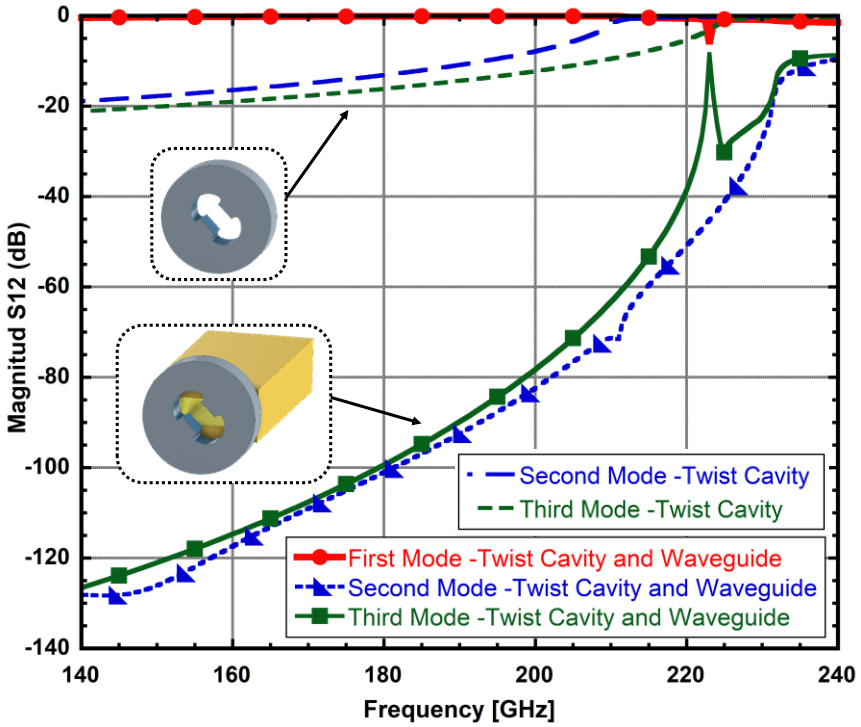

Figure 3.3. *Propagation of the second and third mode for the standalone twist cavity, and the twist cavity connected to a rectangular waveguide. The third mode will introduce a resonance in the response.*

bandwidth of the waveguide twist. A second conclusion can be formulated by analyzing the mode relations in the twist and rectangular waveguide. When the first mode of the twist cavity is excited on the input port, the TE_{10} mode is observed at the rectangular waveguide output. This relation proves its role in the field rotation process.

Simulated performance

The operational bandwidth was maximized by carefully positioning the third mode resonance outside the frequency of operation. The simulation results are illustrated in Figure 3.4.

The twist was simulated with the full-wave 3-D simulator Ansys HFSS [64]. The simulation shows a return loss better than -20 dB over most of the operation band, which implies a 44% fractional bandwidth. In addition, the insertion loss is predicted to be below 0.3 dB for the whole frequency range.

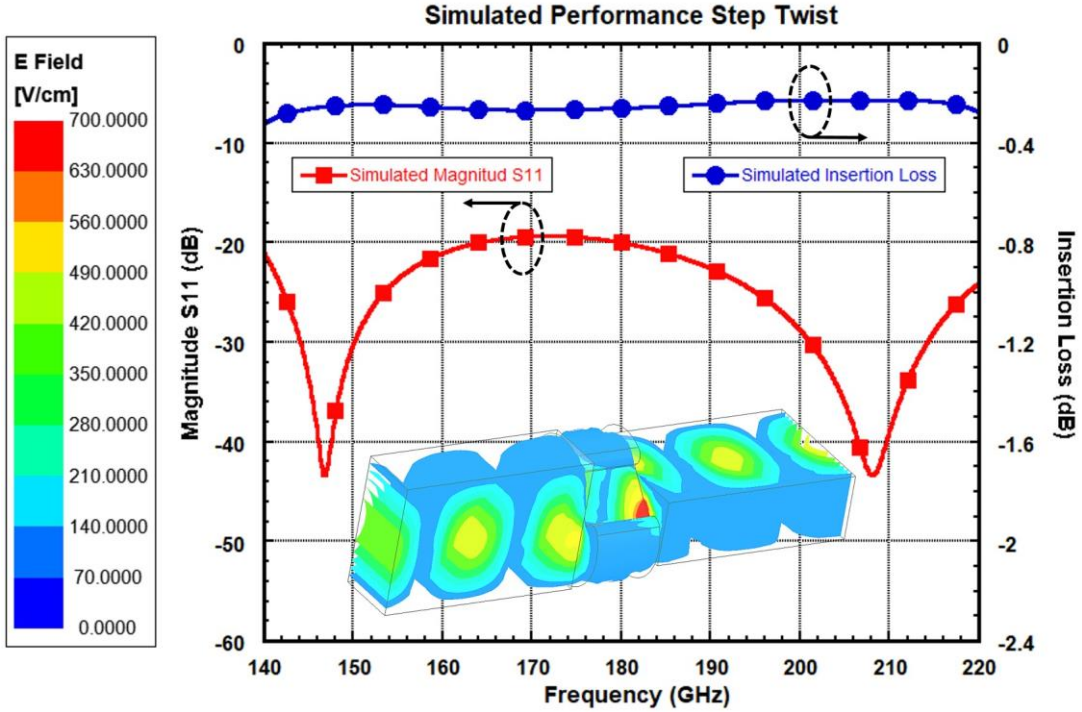

Figure 3.4. *Simulated Performance for the desing twist presented in [Paper A]. The magnitude E-field colour representation shows the field rotation process.*

Section 3.2 - Measurement Setup

The proposed waveguide twist was characterized using Keysight PNA-X 5242 and Virginia Diodes frequency extension modules WR-5.1 with standard TRL calibration. The extension modules should be rotated 90° to account for the twist rotation. Unfortunately, the calibration cannot be performed in this position. Therefore, the setup should be disturbed after calibration to rotate one extension module, which affects the overall precision of the measurements. In order to preserve the measurement accuracy, an additional 90° continuous twist [6] was employed. The continuous twist was positioned at one of the ports providing an additional 90° field rotation. The S matrix of this continuous twist was fully characterized in advance and later de-embedded by software. As a consequence, the physical rotation of the module is avoided during the step twist measurement. In Figure 3.5a, the measurement setup is illustrated. Furthermore, the fabricated step twist and the continuous twist employed in the measurements are depicted in Figure 3.5b. From the picture, it is observed the remarkable difference in thickness between both twists.

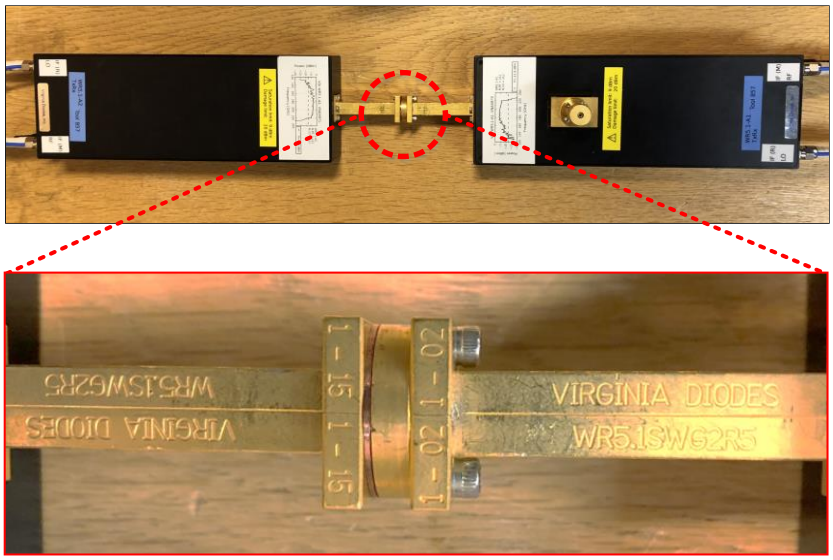

(a)

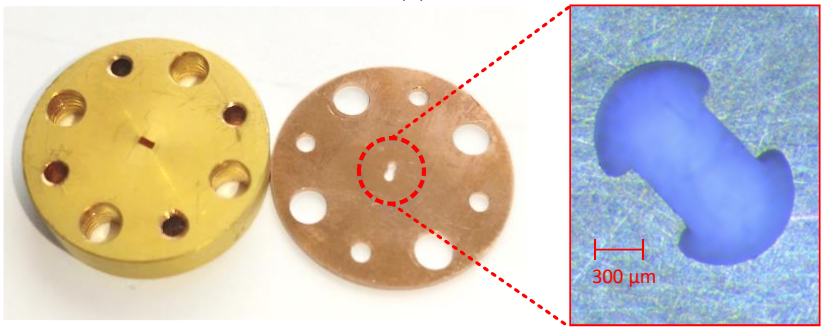

(b)

Figure 3.5. *Mesurement setup and fabricated twist. (a) Mesurement setup (b) Continuos twist (left) and fabricated twist (right). The thicknesses are 4 mm and 660µm, respectively. The fabricated twist is displayed on the left.*

Section 4.3 - Results and Discussion

The measured performance of the fabricated step twist is compared with the simulation in Figure 3.6. The continuous twist response is displayed in the same graph for the sake of comparison.

From the graphs, it can be seen that the experimental data was found in good agreement with the simulation. Although the return loss of the continuous twist is better than the fabricated twist for most of the band, its insertion loss is in the same order. This result implies that a notable bandwidth with minimum insertion loss and a reasonable 20dB return loss can be achieved with the highly compact step twist, which is 6.5 times thinner than the bulky continuous twist.

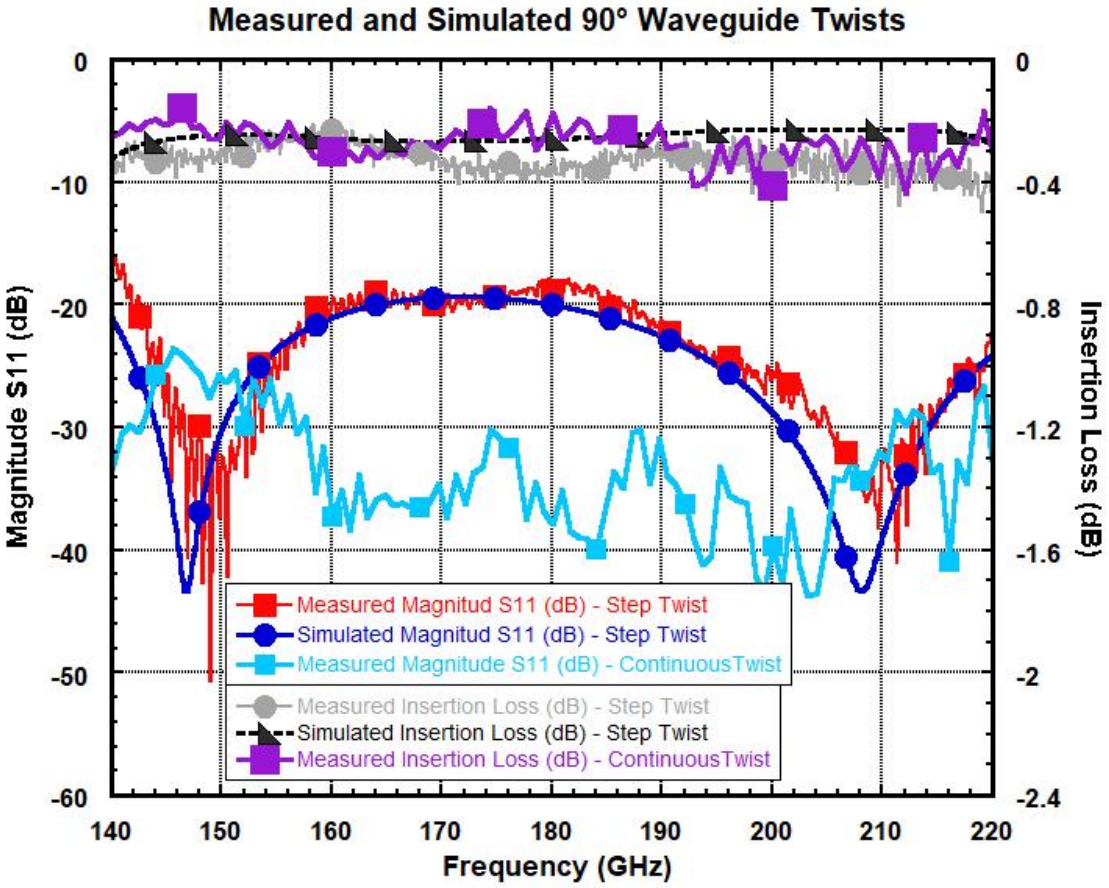

Figure 3.6. *Measured and simulated scattering parameters for fabricated twist and continuous twist.*

The twist proposed in [Paper A] is further compared with the state-of-the-art 90° waveguide twist found in the literature in Table 3.1. From the table, it is seen that the proposed waveguide twist covers a full waveguide band, i.e. 44% bandwidth, with the lower insertion loss and thickness. Although the designs presented in [31] and [60] achieved an excellent performance, their compactness is compromised since they are integrated into a split block. Moreover, the devices explored in [40] and [41] include multiple sharp corners, increasing the fabrication complexity.

Table 3.1 - State of the art comparison of 90° Twists							
Ref	**Frequency [GHz]**	**Franctional Bandwidth**	**Length [λ_g]**	**IL [dB]**	**RL [dB]**	**Geometry**	**Comment**
[6]	140-220	44%	1.8	~0.2	30		Continuous Twist -Fabricated by Electroforming.
[41]	220-320	37%	> 4	0.5	~20	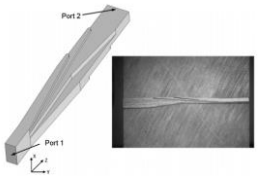	Continuous Twist -Fabricated by direct milling.
	500-700	33%	Not reported	2.5	20		
[33]	75-110	37%	1.12	0.11	25	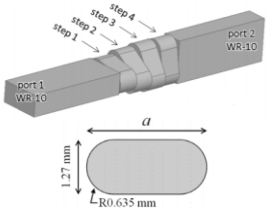	Multistep Twist -Fabricated by direct milling.
[40]	600-750	22%	0.43	0.5	20	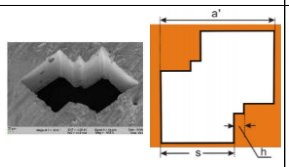	Single step Twist -Fabricated by micromachining.
[60]	220-330	40%	8.75	0.6	20	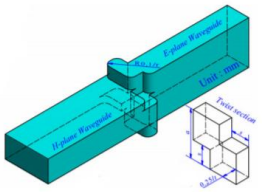	Single step Twist integrated in split block - Fabricated by direct milling.
[31]	220-330	40%	18.14	1	25	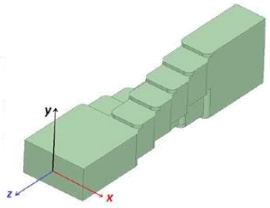	Multistep Twist integrated in split block - Fabricated by direct milling.
[Paper A]	**140-220**	**44%**	**0.3**	**0.4**	**~20**	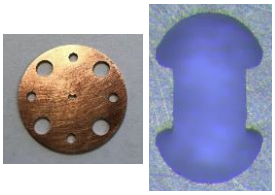	Single step Twist -Fabricated by direct milling.

IL: Insertion Loss **RL:** Reflection Loss $\boldsymbol{\lambda_G}$: guided wavelength.

From the comparison, it becomes clear that the twist proposed in [Paper A] combines a highly compact design with a remarkable fractional bandwidth and minimum losses. Moreover, the absence of sharp corners makes the design suitable for standard milling techniques at least up to 220 GHz. Furthermore, the presented design can be easily scaled down to lower frequency, extending its applicability to a large number of broadband highly integrated waveguide systems.

Chapter 4 - The Substrateless Finlines

The substrateless finline is a novel type of unilateral finline where the substrate between the conductive fins has been completely removed, as shown in Figure 4.1. Meanwhile, the substrate under the fins is preserved. The substrate removal addresses two fundamental problems of waveguides to finlines transitions, i.e. the dielectric losses on the substrate and the impedance matching over large bandwidths. As discussed in Section 2.3, the impedance match of finline transitions is usually compromised by the discontinuity between the dielectric slab and the waveguide. In contrast, the substrateless finline introduces the dielectric slab gradually, which dramatically improves the matching with the waveguide and the resulting bandwidth of the transition. Therefore, substrateless finlines could potentially be employed for wideband designs. In this work, the development of this novel transmission line was intended for wideband cryogenic mixer design in the frequency range 211-375 GHz.

Figure 4.2 depicts the E-field distribution in a waveguide to substrateless finline transition. It is seen how the fundamental waveguide mode TE_{10} is transformed into a finline mode. Since this field distribution is identical to the slotline mode, the electromagnetic energy can be naturally coupled later to a slotline.

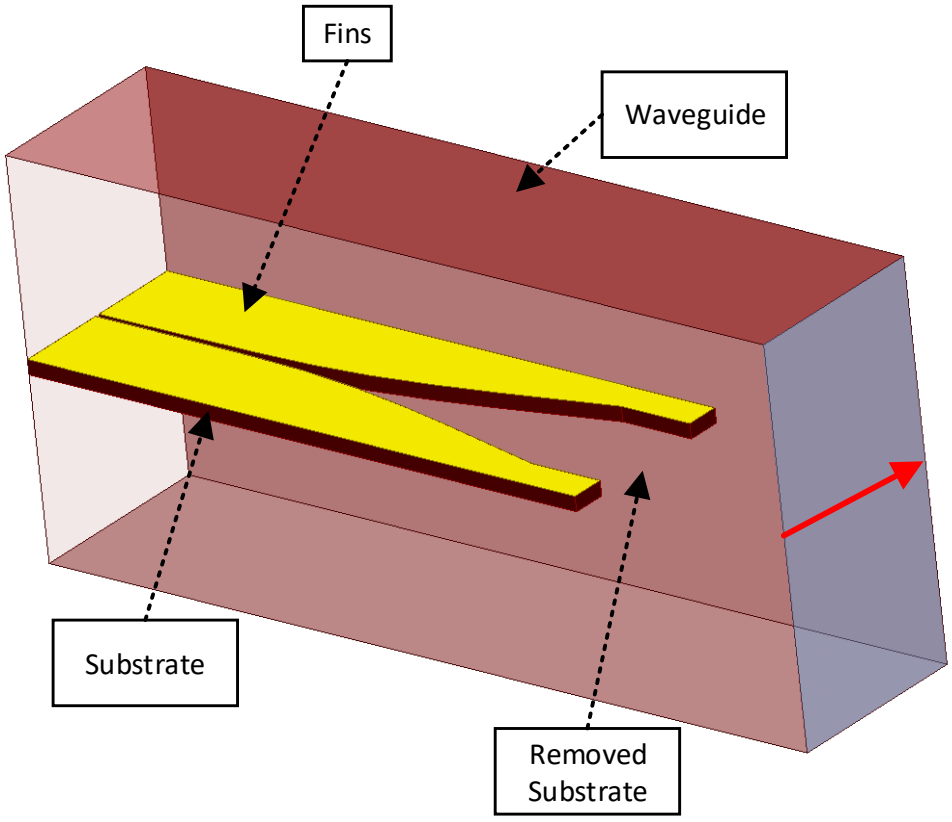

Figure 4.1. *Substrateless Finline waveguide to substrate transition. Note that the substrate enclosed by the conducting fins has been removed. The red arrow indicates the E-field orientation in the waveguide input.*

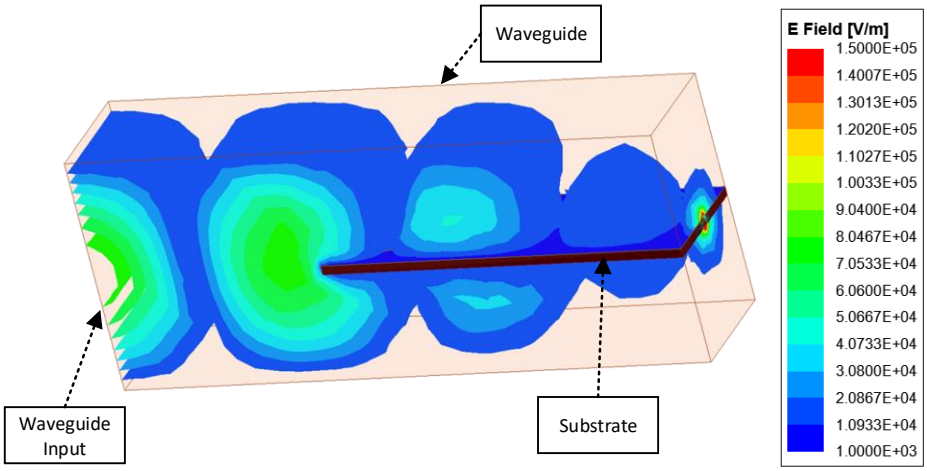

Figure 4.2. *E-field magnitude distribution in a waveguide to substrateless finline transition. The waveguide input is excited with* TE_{10} *mode.*

Section 4.1 - Design of Substrateless Finlines

The taper shape defines the performance of waveguide to finline transitions. In the last decades, several methods for finline taper design have been proposed and tested [61-63]. Nevertheless, these methods have been specially formulated for regular finlines where the substrate between the fins has not been removed. Therefore, in this work, a new method for designing substrateless finline tapers was investigated and presented in [Paper B].

An arbitrary finline taper profile can be generated if the characteristic impedance and the guided wavelength functions are known. The relations between impedance, guided wavelength and fin-gap size can be explored with the help of the full-wave 3-D simulator Ansys HFSS [64]. Employing a single section of substrateless finline, the main parameters of the substrateless finline can be investigated and mapped for different fin-gap. Afterwards, the mapped values can be used to create polynomial approximations that relate the different parameters. However, it should be noted that the approximations produced with this method are only applicable to the conditions established in the simulation. In particular, it is crucial to define the dielectric slab characteristics, i.e. dielectric constant and thickness, since the substrateless finline impedance depends on these values. In this work, float-zone silicon of 30 µm thickness was chosen as the finline substrate. The selection of float-zone silicon was motivated by its low loss at cryogenic temperatures. Moreover, the maturity of the Si etching technology allows removing of the substrate easily. Regarding the thickness of the Si substrate, 30 µm was selected to prevent substrate modes from propagating in the structure [65]. Moreover, the silicon substrate was enclosed by an 800 µm x 400 µm waveguide. This waveguide size completely covers the frequency range which was targeted in the design, i.e. 211-375 GHz.

Once the substrate and frequency range were selected, substrateless finline for fin-gaps ranging from 4 to 400 µm were simulated. Therefore, the impedance and guide lambda vs. fin-gap was obtained. This data was employed to develop polynomial approximation functions, which can be used for multi-step transformer design, as discussed in the next section. A similar procedure was performed for characterizing superconducting slotlines.

Section 4.2 - Waveguide to Substrate transition employing Substrateless Finlines

The approximations for characteristic impedance and guided lambda were employed to design a waveguide to substrate transition for 211-375 GHz frequency range. The transition transforms the nearly 500 Ω of a full-height waveguide into a 70 Ω superconducting slotline. As illustrated in Figure 4.3, the impedance transformation was achieved with an 8 steps transformation that includes 2 Chebyshev transformers; the first 5 steps, S1 to S5, consist of a substrateless finline that matched the waveguide impedance to 108 Ω, while the remaining 3 slotline steps, S6 to S8, further reduce the impedance to 70 Ω.

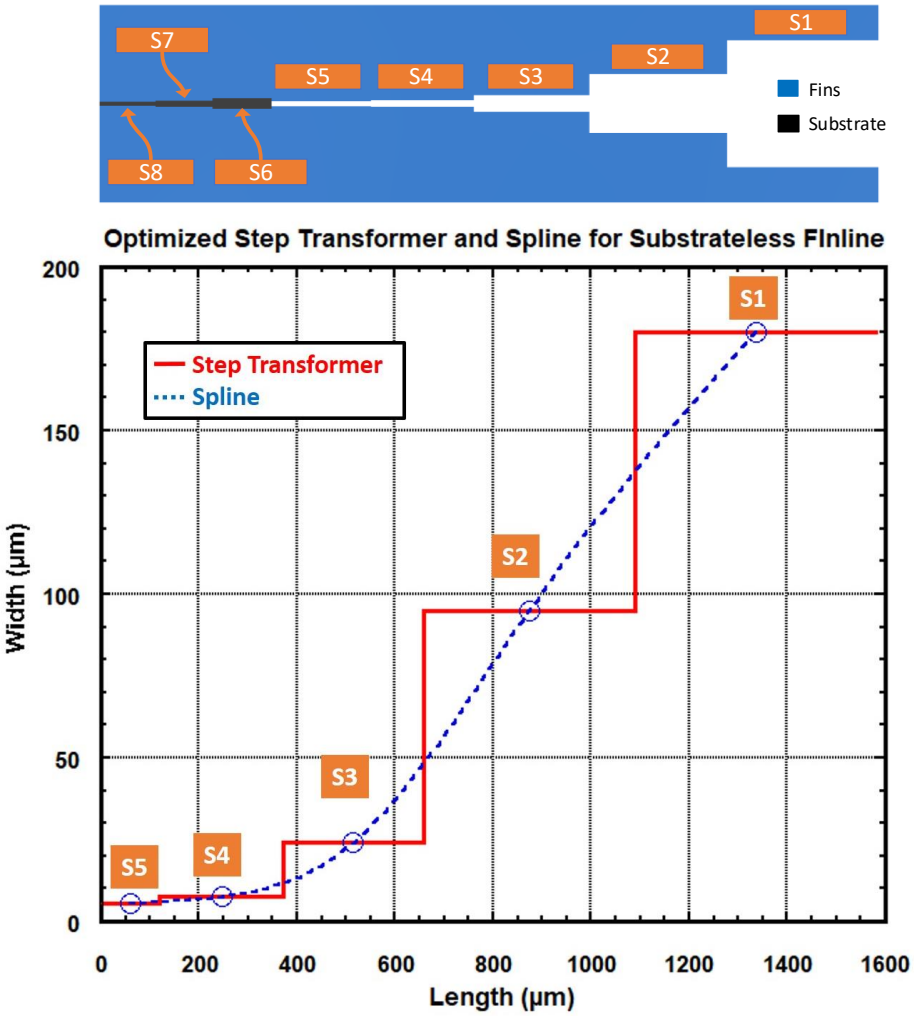

Figure 4.3. *Design of waveguide to substrate transition. Top: Substrateless Finline and superconducting slotline transformer. The different steps of the full transformation are depicted. Bottom: Optimized step transformer and resulting finline taper (spline).*

The taper shown in Figure 4.3 was obtained after drawing a spline curve through the centre of each step. The spline definition generates a smoother impedance transition since it reduces the effect of step discontinuities in the response [66].

Employing the finline taper and the superconducting slotline transformer, the waveguide to substrate transition illustrated in Figure 4.4a was designed. The transition incorporates superconducting Nb fins deposited over 30 µm Si substrate. Moreover, the Nb fins are grounded to the copper block through Au beamleads that extend 100 µm beyond the substrate. The Au beamleads overlaps the superconducting fins and follow a similar spline, but they are offset from the Nb edge to avoid losses in the Au. When the waveguide split block is closed, the beamleads are clamped and pressed between the two halves, as shown in Figure 4.4a and c.

Consequently, the device is supported only by the beamleads and the substrate is suspended inside the waveguide block. It is important to note that the waveguide width was increased from 400 µm

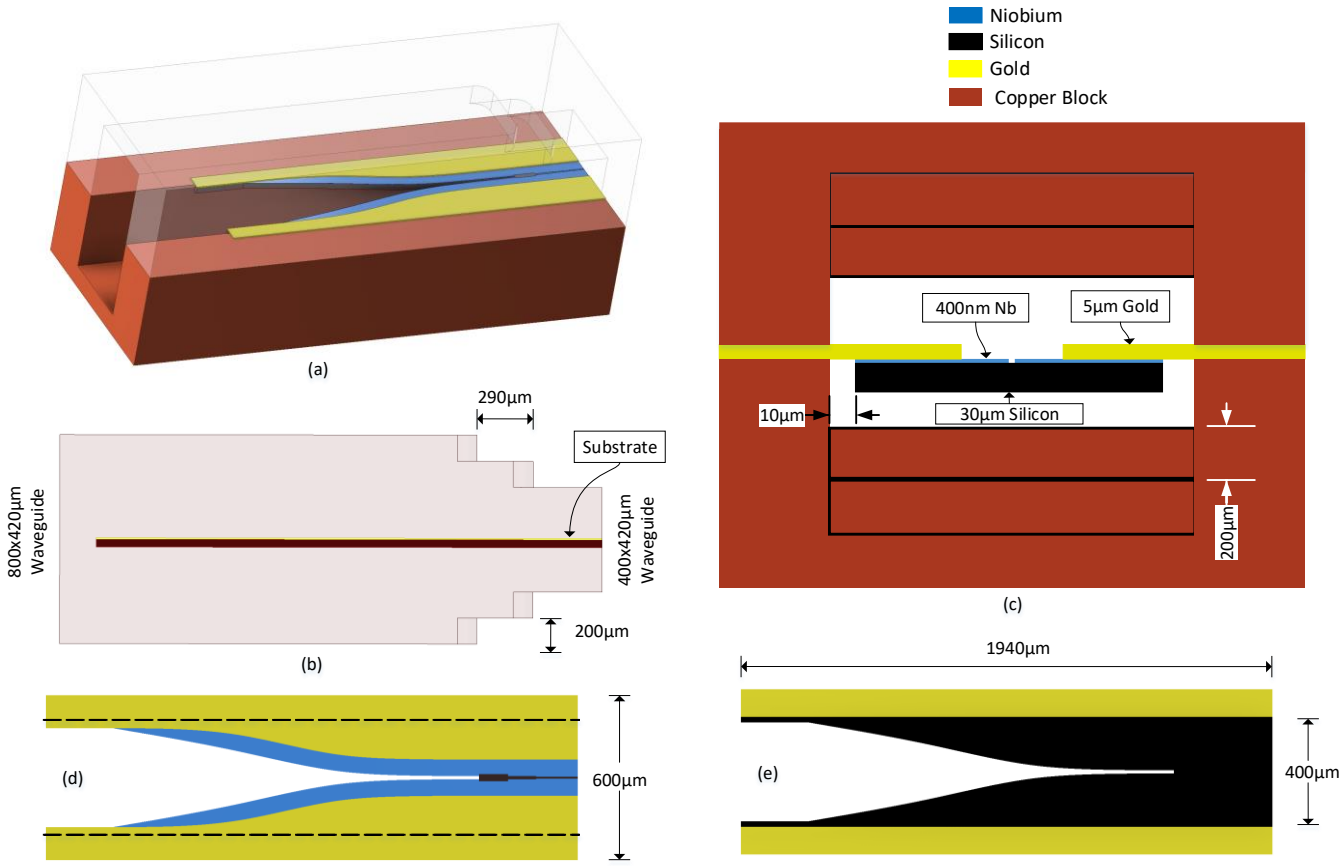

Figure 4.4. *Waveguide to substrate transition. (a) Transition mounted in the block. (b) Lateral view of the structure mounted in the waveguide. (c) Transition viewed from slotline side. The different material thicknesses are appreciated. For the sake of clarity, this image is shown not to scale. (d) Top view of the transition. Au beamleads extend by 100 µm from each side of the silicon substrate. The dashed lines illustrate the waveguide dimension. (e) The bottom view reveals the profile of the silicon substrate and its overall length.*

to 420 µm. This additional 20 µm facilitates the mounting of the device since a 10 µm gap is created between the substrate and the waveguide wall.

As depicted in Figure 4.4b and c, the block height is reduced in 2 equal steps to obtain the subcritical dimension 400x420 µm. This waveguide dimension prevents the propagation of unwanted waveguide modes in the frequency of operation. The waveguide height variation is introduced when the field has already concentrated between the fins, as shown in Figure 4.4b. Thus, the change of waveguide height has almost no effect on the impedance of the transition.

It is important to remark that a tolerance analysis was performed to investigate the sensitivity of the different parameters of the device. It was concluded that the fabrication precision was required to be ±1 µm for the step widths and ±5 µm for the step longitudes. A standard microfabrication process can achieve this precision.

Back-to-Back Structure Superconducting Simulation

Since the S parameter characterization systems at the targeted frequency range 211-375 GHz make use of waveguide extenders, it was developed a structure composed of two transitions in a back-to-back arrangement for mounting in a split block waveguide. With a back-to-back structure, the simulations and measurements can be easily compared. The back-to-back structure is shown in Figure 4.5a. From the image, it can be seen that silicon tips have been added to the finline structures. These silicon tips, which rest inside pockets in the block, facilitate handling and alignment of the back-to-back finline sample.

The electromagnetic performance of the back-to-back structure at 4 K was simulated in Ansys HFSS employing two different approaches. Firstly, the superconducting Nb layer was simulated as a perfect conductor (PEC). Secondly, the complex surface impedance of the superconductor was calculated following the BCS theory. Moreover, the surface impedance values were computed for 450 nm of Nb in the frequency range 211-375 GHz. Afterwards, the complex impedance was applied as an impedance boundary to the fins. This procedure was based on the superconductor simulation detailed in [67] and the method proposed in [68] for the superconducting microstrips simulation.

The PEC and superconducting simulations are compared in Figure 4.5b. It is seen that both simulations predict an insertion loss of less than 0.6 dB, and a return loss better than 15 dB over the whole band, i.e. 211-375 GHz. However, the superconducting approximation response seems to be shifted to higher frequencies. This shift may be explained by the reactive component of the surface impedance, which is not present in the PEC approximation. Nevertheless, the agreement of the simulations indicates that the functions developed in [Paper B] give a reasonable approximation for substrateless finline and superconducting slotline design. In the case of superconducting finlines and slotlines, the magnetic field penetrates into the superconductor from both faces of the superconducting thin film that forms the fins. Therefore, the PEC approximations developed in [Paper B] will remain valid as far as the fins are much thicker than twice the London penetration depth λ_L of the superconducting material, e.g. 180 nm for a thin-film Nb layer.

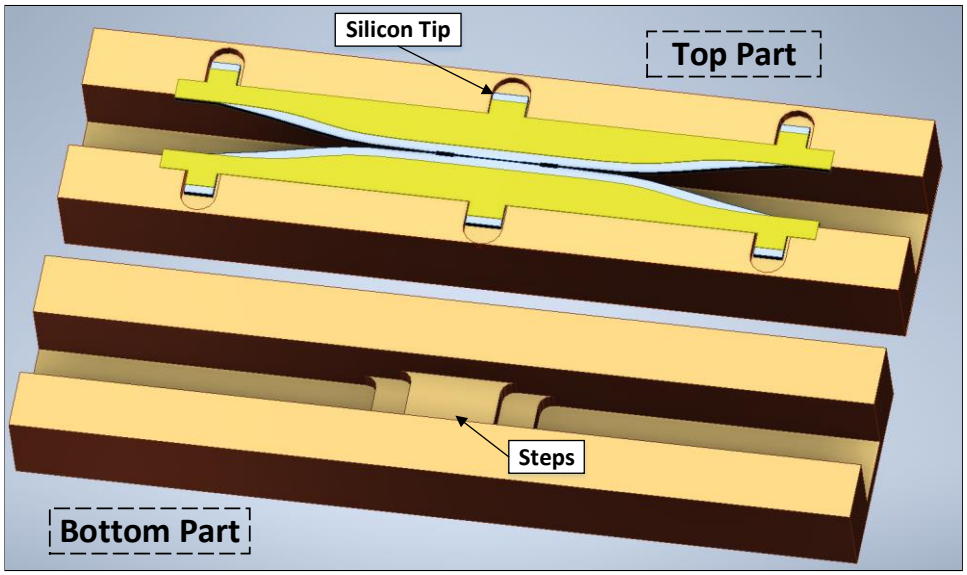

(a)

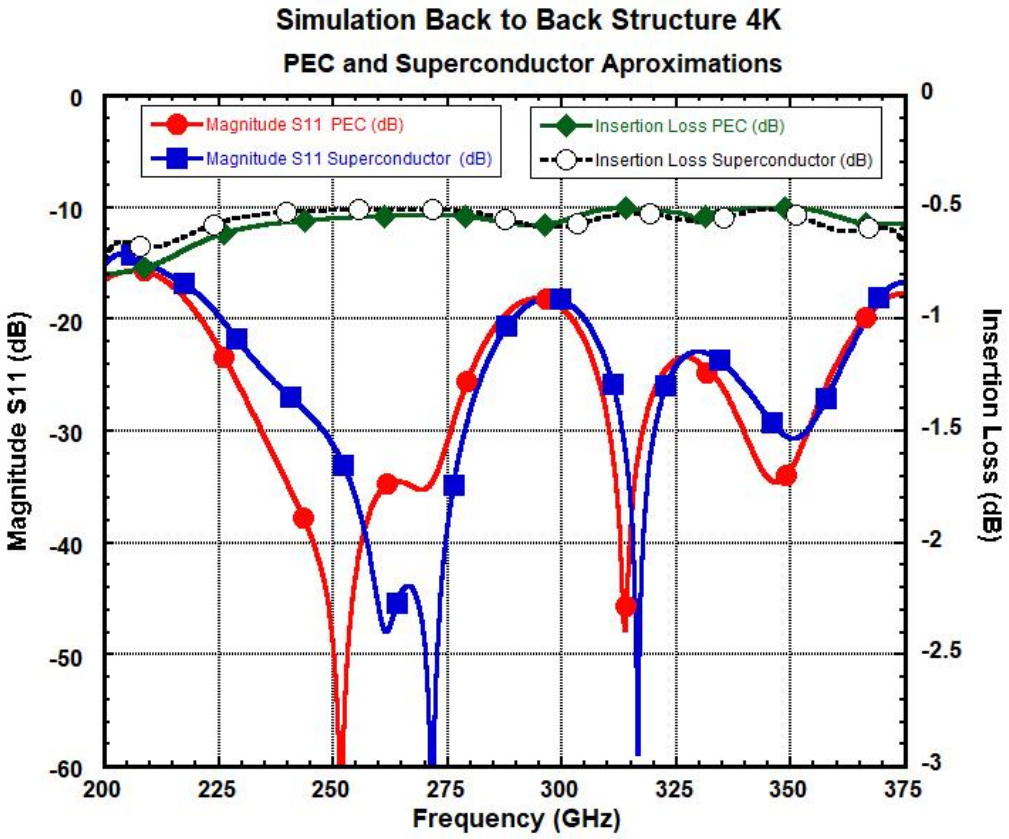

(b)

Figure 4.5. *Back to Back transition. (a) Transition mounted in the block. The upper and lower halves of the block are depicted separately. (b) S parameter simulation of back-to-back structure employing PEC and Superconductor approximations.*

Section 4.3 - Bending of the fabricated Structure

The samples were fabricated following the process presented in [Paper B]. After the samples were released, they were inspected under the microscope. From this analysis, it was appreciated that the back-to-back structures were bent. The bending was further analyzed by employing an optical 3D profilometer. The inspection results depicted in Figure 4.6 show that the structure symmetrically bends along the X-axis. This deformation may be the result of the fabrication process. In particular, the Nb layer is deposited with a compressive stress of about 200 to 300 MPa, which may cause the bending of the finline structure. Stress-free Nb films are hard to accurately achieved, while tensile stressed films have the substantial disadvantage of worse adhesion and porous structure, which degrade their superconductive properties [69]. Therefore, compressively stressed Nb film is

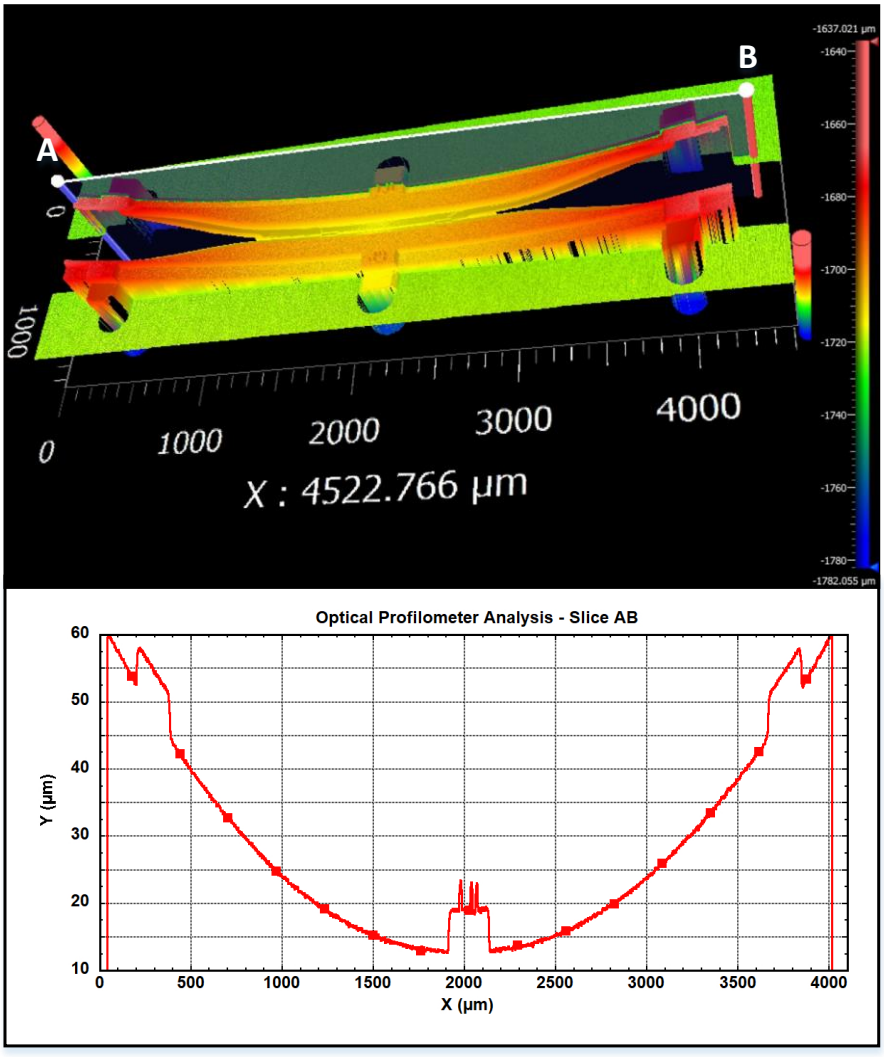

Figure 4.6. *Profile analysis of the fabricated back-to-back structure. The 3D representation clearly show the structure is bending along the X axis. The profile graph for the slice "A-B" shows that the structure is bended 55 µm with respect to its center.*

employed as it provides the highest superconducting properties, as well as having the least developed surface topography for the film [69].

The deformation of the structure complicates the correct mounting of the samples in the block. Nevertheless, the considerable flexibility of the thin silicon substrate allowed to reshape of the back-to-back structure. With the help of a wire bonding machine, the beamleads were carefully pressed against the block surface to flatten the structure. It is important to remark that the bonding wire was not required during this process. In Figure 4.7, it can be observed the places where the bonding wedge pressed the beamleads. This method allowed to flatten and, by that, ease mounting of the devices into the block.

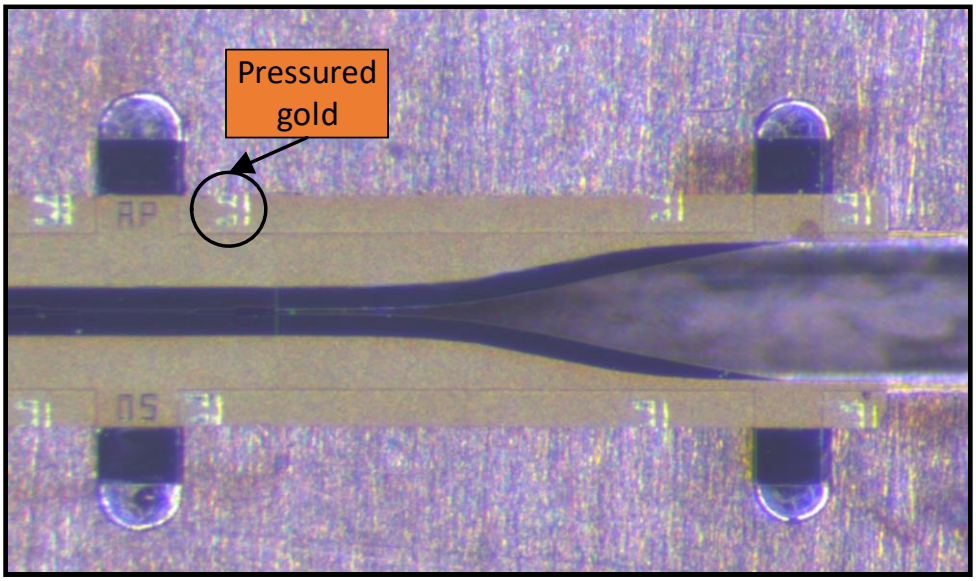

Figure 4.7. *Flattened structure mounted on the lower half of the split block. The marks of the bonding wedge are visible over the finline beamleads.*

Section 4.4 - Cryogenic Measurements of Substrateless Finline

The measurement of the fabricated samples was performed with the help of the setup shown in Figure 4.8. It consists of a Keysight PNA-X 5242A, a 4 K closed-cycle cryostat where the device under test (DUT) was cooled, and a pair of frequency extension modules Virginia Diode Inc. [70]. Due to the considerable fractional bandwidth of the DUT, three pairs of extension modules for different frequency ranges were employed in the measurements, i.e. WR-5.1 (140-220 GHz), WR3.4 (220-330 GHz), and WR2.2 (330-500 GHz). However, the cryostat input waveguide was WR-10 (75-110 GHz), hence a pair of adapters were employed to transform the waveguide sizes from WR-10 to the required waveguide dimension of the extension modules as depicted in Figure 4.8b. These adapters allow to overmode the WR-10 waveguide chain. Moreover, since the DUT

waveguide size is 800x420 um, an additional pair of adapters were located at the 4K stage inside the cryostat, as illustrated by Figure 4.8c.

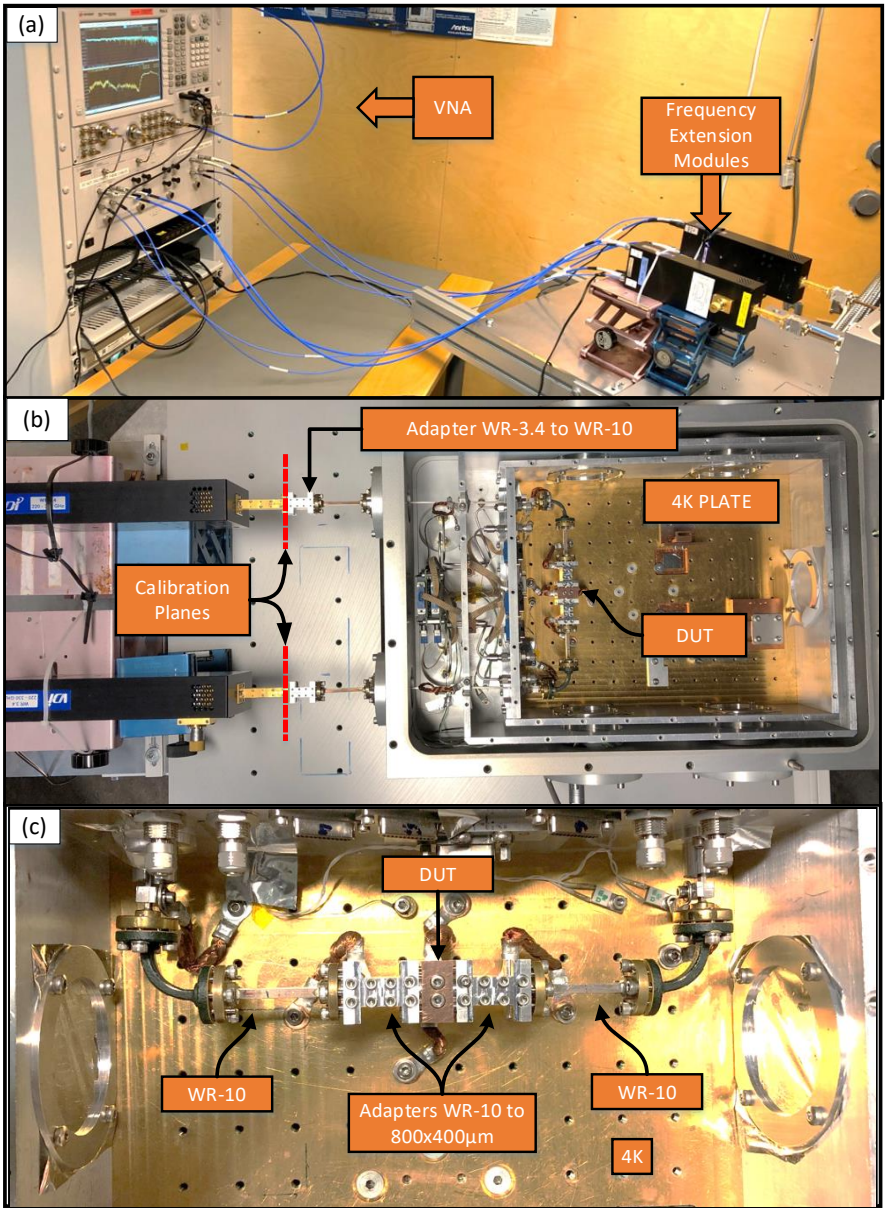

Figure 4.8. *Measurement setup. (a) WR-3.4 frequency extension modules and VNA (b) The extension modules are connected to the WR-10 waveguide chain using adapters. The calibration plane is located outside the cryostat. (c) Waveguide chain inside the cryostat.*

The major challenge in measuring S parameters at cryogenic temperatures lies in the calibration inside a cryostat, especially at high frequencies where waveguide systems are employed. The reduction of the waveguide chain losses during cooling dramatically affects the reference planes

calibrated at warm inside the cryostat since the warm calibration overestimates the losses. The shift of the calibration planes could be corrected by measuring a short circuit standard at 4K, as described in [71]. This method for cryogenic measurements is frequently applied at lower frequencies where coaxial cables are employed. Nonetheless, it is not practical at higher frequencies due to the waveguide chain's thermal contraction. This shrinking is comparable to the guided wavelength, thus, it is not possible to accurately correct the room temperature calibrations. Therefore, an alternative measurement procedure using waveguide frequency extension modules was developed to characterize the insertion loss of back-to-back substrateless finline structures. A standard warm TRL calibration was applied to position the calibration planes at the input of the cryostat, as depicted in Figure 4.8b. This calibration served to measure the DUT and a waveguide thru at 4K and 10K. The waveguide chain was identical for both measurements, which allows the comparison of the DUT insertion loss with the waveguide Thru. As a result, the relative insertion loss of the DUT was obtained and compared with the simulation. The same procedure was repeated for the three frequency bands.

Figure 4.9 shows the comparison between the simulated and measured performance of the fabricated back-to-back transition. From the graph, it can be seen that the experimental data was found in good agreement with the simulation. The measured back-to-back insertion loss at 4K is less than 1 dB almost over the entire frequency range. Meanwhile, the losses triple above the superconducting transition temperature, i.e., 9.3K for Nb. Although the results are consistent with the simulation for the lower frequencies, experimental data deviate for the higher frequency end. These deviations may be explained by minor differences in the waveguide chains and fabrication.

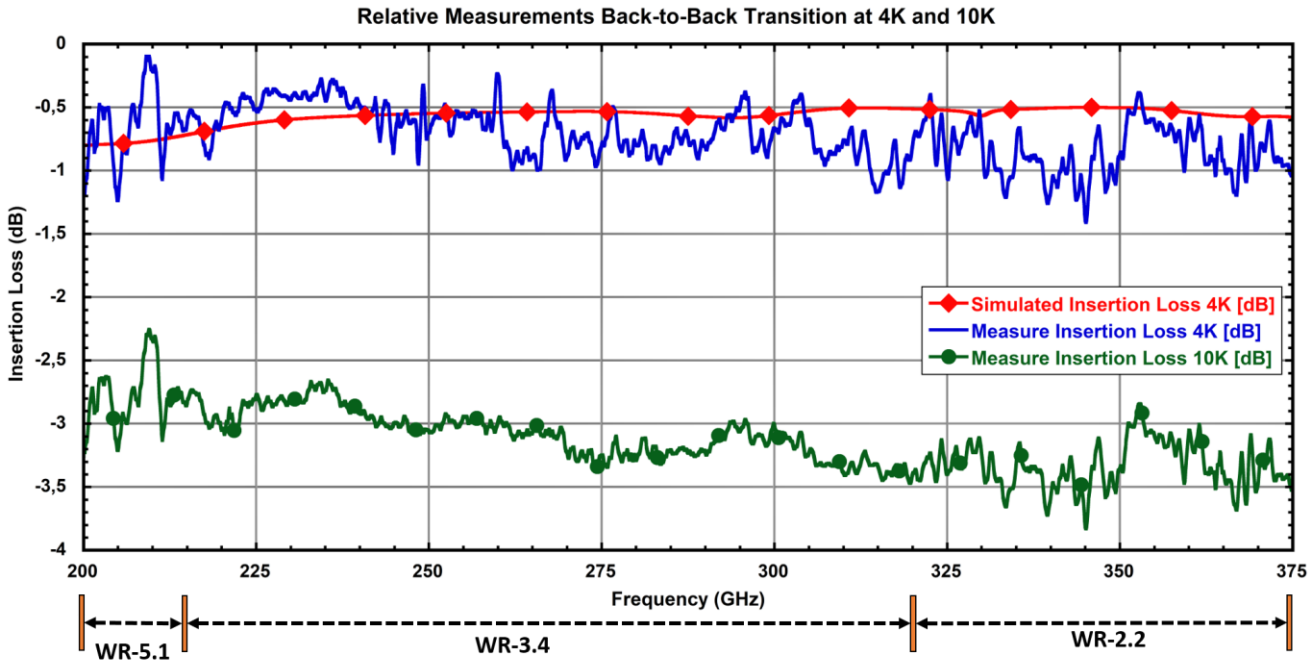

Figure 4.9. *Measured and simulated insertion loss for 4K together with the measured frequency bands. The losses above the transition temperature for Nb are also plotted.*

Section 4.5 - State of the Art Comparison

The novel substrateless finlines presented in [Paper B] achieved a remarkable fractional bandwidth of 55%. Table 4.1 shows the state-of-the-art waveguide to substrate transitions intended for THz receivers. From the table, it is evident that the proposed transition stands out not only for its bandwidth but also for its direct measurement at cryogenic temperatures. The complexity of the direct cryogenic measurements made the low-frequency scale model the preferred method for design verification. Moreover, this verification is done at room temperature. Nonetheless, this method presents a series of significant limitations. For instance, during the cooling cycle, the

TABLE 4.1 STATE OF THE ART WAVEGUIDE TO SUBSTRATE TRANSITIONS

Reference	Transition Tipe	Intended Frequency Band	Fractional BW @ 15 dB Return Loss	Insertion Loss [dB]	Measurement Method	Image
[72]	Radial Probe to microstrip	375-500	~30%	0.15	Scale Model Verification - Warm	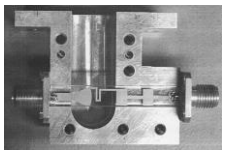
[73]	Radial Probe to microstrip	140-220	44.4%	0.45	Estimation from Cryogenic Measurement	
[43]	Radial Probe to microstrip	270-430	45.7%	Not Reported	Scale Model Verification - Warm	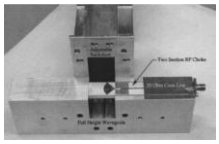
[74]	Radial Probe to microstrip	700-1100	44.4%	Not Reported	Simulation	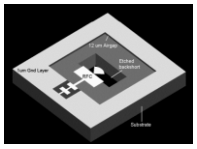
[47]	Dual-dipole antenna to microstrip	580-800	31.8%	2	Scale Model Verification - Warm	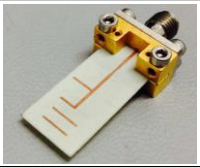
[55]	Unilateral Finline to slotline	550-750	30.7%	Negligible	Simulation	
[75]	Unilateral Finline to slotline	170-265	38.2%	0.5	Measure Back to Back Transition - Warm	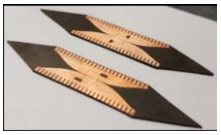
[Paper B]	**Unilateral Substrateless Finline**	**211-375**	**55%**	**~0.5**	**Cryogenic Back to Back Insertion Loss Measurement**	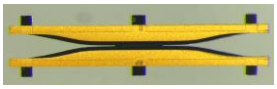

thermal contraction of the various materials and the rise of stress can easily break ultrathin silicon devices. The survival of the device to a cooling cycle cannot be assessed adequately with warm measurements. Furthermore, the impact of the fabrication and mounting tolerances cannot be evaluated with low-frequency scale models. To the best knowledge of the authors, the insertion loss measurement presented in [Paper B] constituted the first verification of a back-to-back structure at cryogenic temperatures.

This ultrawide bandwidth of substrateless finline transitions opens new possibilities for the design of receivers in radio astronomy applications. In particular, the presented substrateless finline allows covering ALMA band 6 (211-275 GHz) and ALMA band 7 (275-375GHz) simultaneously [16]. Nevertheless, the applicability of this new type of finline is not limited to radio astronomy applications, but it can be employed in a wide range of mm and sub-mm applications. For instance, it may be applied in the THz communication systems that have increasingly drawn attention in recent years [5]. Moreover, the design procedure detailed in [Paper B] might be employed for different frequency ranges, making substrateless finlines an attractive solution for a great variety of wideband applications.

Chapter 5 - Ongoing Research: Ultrawideband Slotline to Microstrip Transition for 211-375 GHz based on Marchand Balun

The transition based on Substrateless finlines detailed in Chapter 4 transforms a waveguide impedance into a slotline. Since fabricating slotlines with small characteristic impedances below 10 Ohm is not practical at mm-wave and THz frequencies, most modern SIS mixers rely on other types of transmission line, e.g. thin-film microstrip lines [45]. Therefore, the need for an additional transition step from slotline into microstrip becomes clear. To address this need, the ongoing research is focused on the design, fabrication and cryogenic measurement of a slotline to microstrip transition covering the frequency range 210-375 GHz.

The literature review on existing microstrip to slotline transitions presented in Section 2.4 shows the Marchand baluns as a promising solution due to their compactness and straightforward design. However, to the author's best knowledge, these baluns have not been previously investigated for sub-mm applications. In this chapter, the design and fabrication of a superconducting Marchand balun for future wideband mixer chip design.

Section 5.1 - Transition design

The proposed transition depicted in Figure 5.1 is based on a third-order Chebyshev Marchand balun [56]. The balun consists of a microstrip and a slotline that lie perpendicular to each other. The structure is patterned on top of a 30 µm Si substrate compatible with the finline structure presented in [Paper B]. The slotline and the microstrip are defined by 450 nm of superconducting Nb, and they separated by a layer of 1.3 µm SiO_2. This particular dielectric thickness was chosen to achieve the required impedance while keeping the microstrip width at the level of a few µm, i.e. compatible with the available microfabrication process.

Figure 5.2 outlines the different impedances employed in the transition as an equivalent circuit diagram. The transition transforms a 60 Ohms slotline, referred to as ZoS, into a 45 Ohms microstrip, denominated as ZoM. The transformation is accomplished with two stubs: an open circuit microstrip stub and a short circuit slotline stub, with Z1 and Z2 characteristic impedances, respectively. Besides, Z3 is realized as a $\lambda/4$ slotline section that matches the intersection impedance to ZoS. The procedure to calculate the impedances Z1, Z2 and Z3 are detailed in Appendix I.

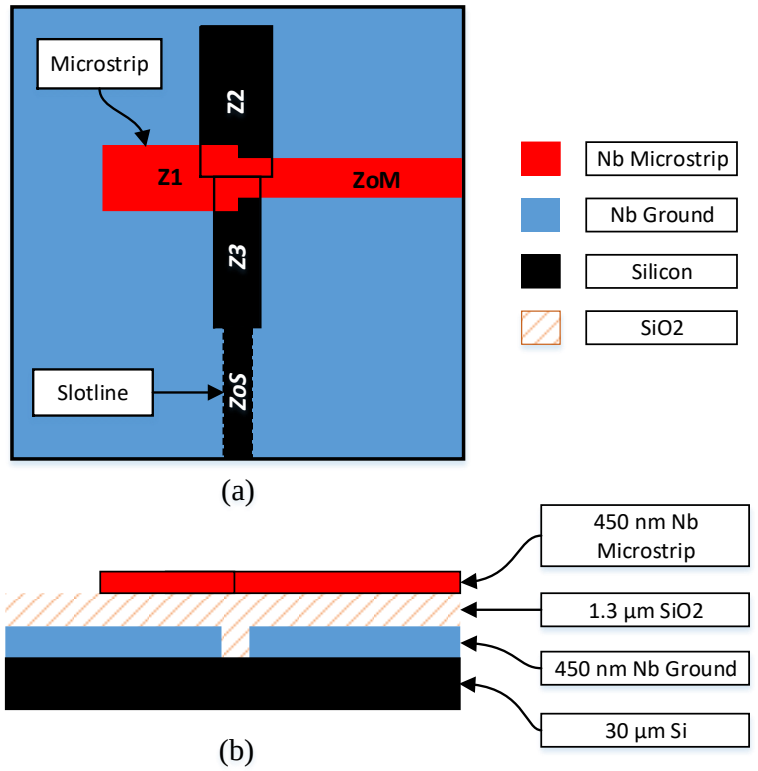

Figure. 5.1. *Proposed slotline to microstrip Marchand Balun transition. (a) Top view of the transition. (b) Lateral view of the structure where the different layers and thicknesses are detailed.*

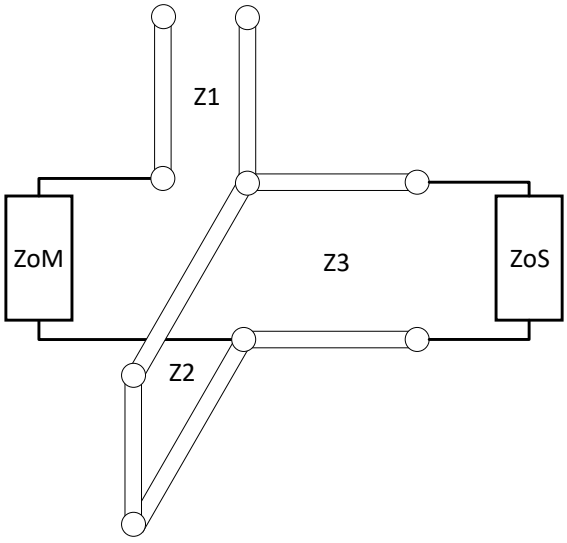

Figure 5.2. *Equivalent circuit diagram of the proposed third order Chebyshev Marchand Balun transition. The microstrip impedance ZoM is 45 Ohm while the slotline impedance ZoS is 60 Ohm. The impedances Z1 and Z3 are realized with slotlines. Meanwhile, the short circuit stub with a characteristic impedance Z2 is realized as a microstrip.*

Section 5.2 – Back-to-Back Electromagnetic Simulation

After the dimensions of the transmission lines were defined, the complete Marchand Balun was simulated and optimized for minimizing the insertion loss in the full-wave 3-D simulator Ansys HFSS [64]. Figure 5.3a shows that the optimization was performed with a back-to-back layout, where both input and output are microstrips. This layout responds to the particular characteristics of the simulator, where microstrips are simpler to excite than slotlines. Moreover, the

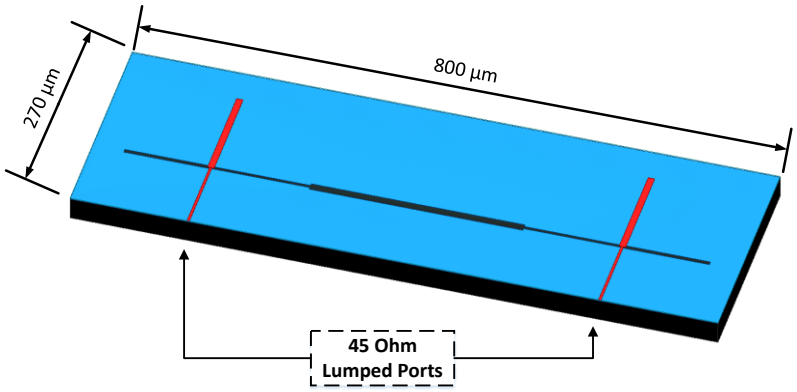

(a)

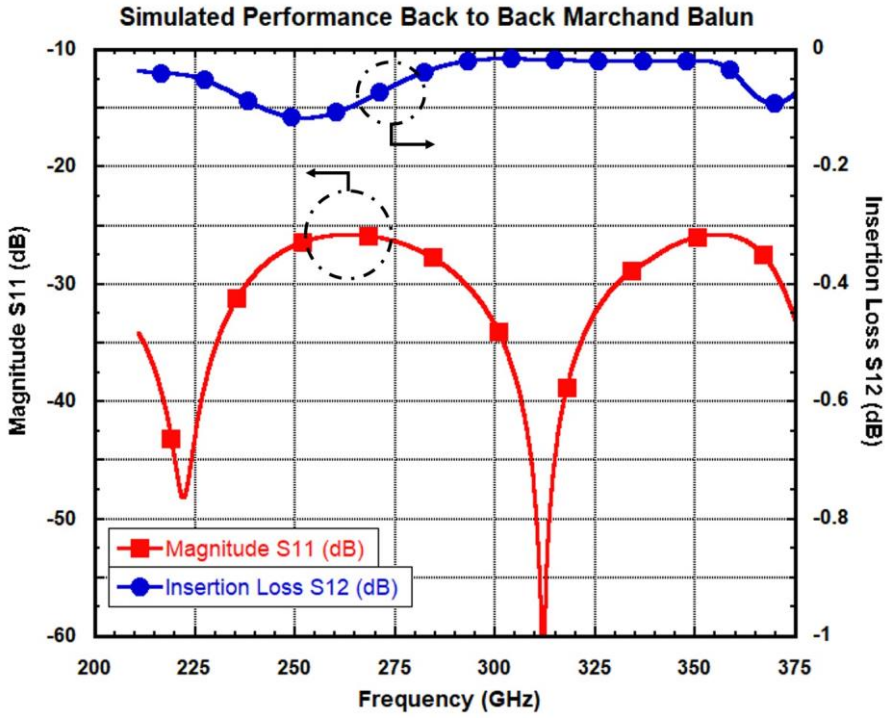

(b)

Figure 5.3. *Electromagnetic Simulation (a) Simulated back-to-back structure. The microstrip ports were excited with 45 Lumped Ports. (b) Simulated S parameters Marchand Balun Transition in a back-to-back arrangement.*

superconducting Nb was simulated as a perfect conductor. This approximation was appropriate since the dielectric thickness is several times the thickness of Nb, i.e. 1.3 µm and 0.45 µm, respectively. Under this condition, the superconducting microstrip impedance resembles a microstrip with perfect conductor electrodes [67, 68].

The simulation results for the back-to-back balun are presented in Figure 5.3b, where the calculated and optimized transition can be compared. The graph shows that the simulated return loss for the optimized back-to-back Marchand Balun is better than 25 dB in the whole band. Furthermore, the insertion loss is above -0.1 dB in the entire frequency range.

Section 5.3 - Test Chip Design

To fabricate and assess the performance of the back-to-back Marchand Balun, the structure must be integrated with a waveguide to microstrip transition. Thus, the back-to-back transition was integrated with E-probes. However, a single probe cannot cover the entire frequency band adequately. Therefore, two versions of the test chip for the frequency range 211-295GHz and 295-375 GHz were designed. A separate probe was designed and optimized for each frequency range. Both test chips included a straight section of microstrip that connects the probe with a 90° microstrip bend terminated in 45 Ohm, i.e. ZoM. The microstrip bend was introduced to accommodate the Marchand Balun transition in a back-to-back layout. The chip is grounded through a 5 µm thick Au beamleads that extend 80 µm beyond the silicon substrate. The beamleads provide an electrical connection between the niobium ground layer and the waveguide block since the gold is clamped and pressed between the two waveguide halves. The waveguide size of the blocks is 800x400 µm to cover the entire frequency range 211-295GHz. The samples were fabricated in house following the procedure detailed in Appendix II.

Section 5.4 - Ongoing Work

The characterization of the test chips at cryogenic temperatures is ongoing. Figure 5.4 illustrates the fabricated chip and the measurement setup. The setup includes waveguide bends with integrated waveguide size adapters from 2540x1270 µm (WR-10) to 800x400 µm. These adapters are employed to connect the waveguide blocks, where the fabricated chips are mounted, to the existing WR-10 waveguide chain of the cryostat. The chips are measured employing the technique described in [Paper B], i.e. the insertion loss is compared with a waveguide thru at 4 K. This approach allows for a straightforward comparison between measurements and simulation.

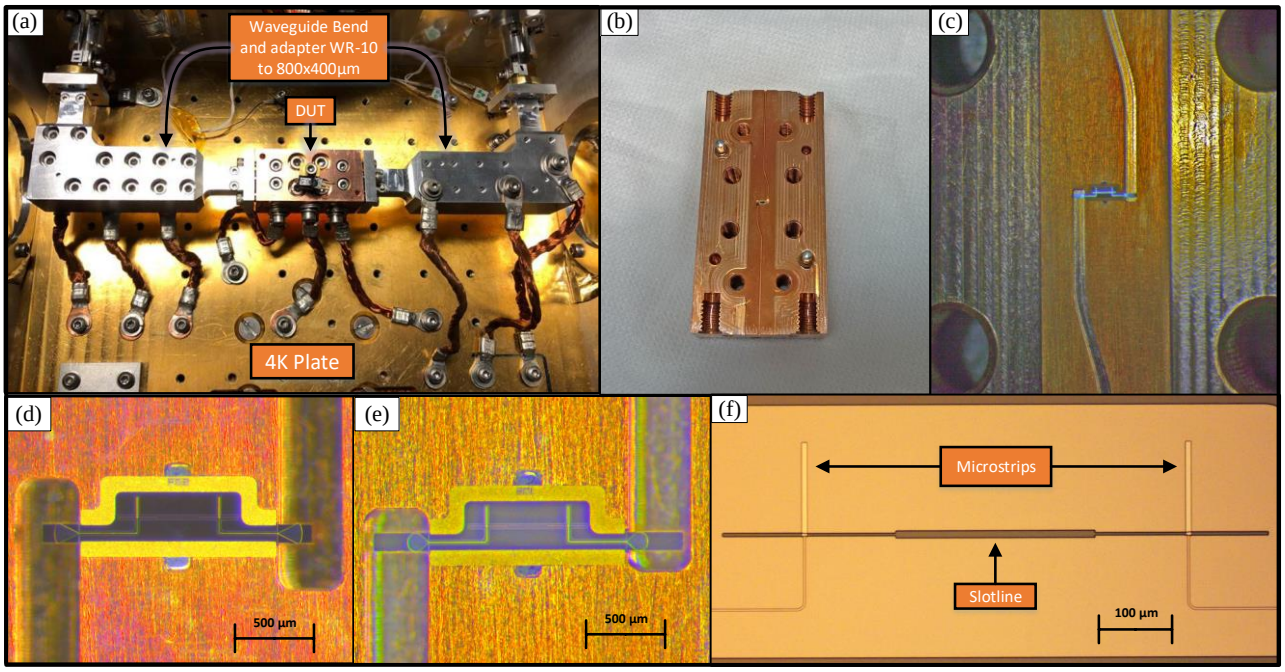

Figure. 5.4. *Measurements setup and fabricated test chips. (a) Waveguide chain mounted inside the cryostat. The DUT fabricated in tellurium copper is connected to the WR10 system through waveguide bends that integrate waveguide adapters. (b) Test Chip mounted in the lower part of the split block. (c) Magnified image of the mounted test chip. The S shaped waveguides are employed to maintain output symmetry. (d) Test Chip covering the lower frequency band (210-295 GHz). (e) Test Chip covering the higher frequency band (295-375 GHz). (f) Detail of the fabricated back-to-back Marchand Balun.*

Chapter 6 - Conclusion and Future Outlook

The next generation of radio astronomy receivers demands a considerable improvement in the RF bandwidths of passive devices. To address this need, a series of ultra-wideband passive devices have been presented in this thesis.

Firstly, a 90° step twist for the frequency range 140-220 GHz was presented. In contrast to existing designs, the twist presented in this work avoids sharp corners, which greatly enhances manufacturability through direct milling without compromising its performance or compactness.

Secondly, a new type of finline was developed, i.e. the substrateless finlines. This novel approach improves the matching with waveguides and reduces the overall losses in the substrate. Consequently, substrateless finlines are an attractive solution for the design of ultra-wideband waveguide to substrate transitions. In this thesis, a waveguide to substrate transition with 55% fractional bandwidth (211-375 GHz) was designed, simulated and measured at cryogenic temperatures. To the authors' best knowledge, the insertion loss measurement presented in this work constituted the first verification of a back-to-back structure at cryogenic temperatures.

The need for further transition from slotline to microstrip motivates the ongoing research on Marchand Baluns. In this work, a slotline to microstrip transition was designed and simulated for the frequency range 211-375 GHz. The simulations showed promising results, and characterization at 4 K is ongoing.

Figure 6.1a shows a conceptual integration of the Marchand Balun with substrateless finline to design a waveguide to microstrip transition. This transition could be employed for the future design of broadband SIS mixers receivers. In Figure 6.1b, a conceptual block diagram for a sideband separating receiver is depicted. In the block diagram, the RF and LO signals are transferred to the substrate with the waveguide to microstrip transition shown in Figure 6.1a. Moreover, the RF 90° hybrid and power divider could be integrated on the same chip.

Even though the devices presented in this work were meant for radio astronomy receivers, other applications at THz frequencies could possibly benefit from this development. Furthermore, the presented designs can be easily scaled down to lower frequencies, extending their applicability to a large number of broadband systems.

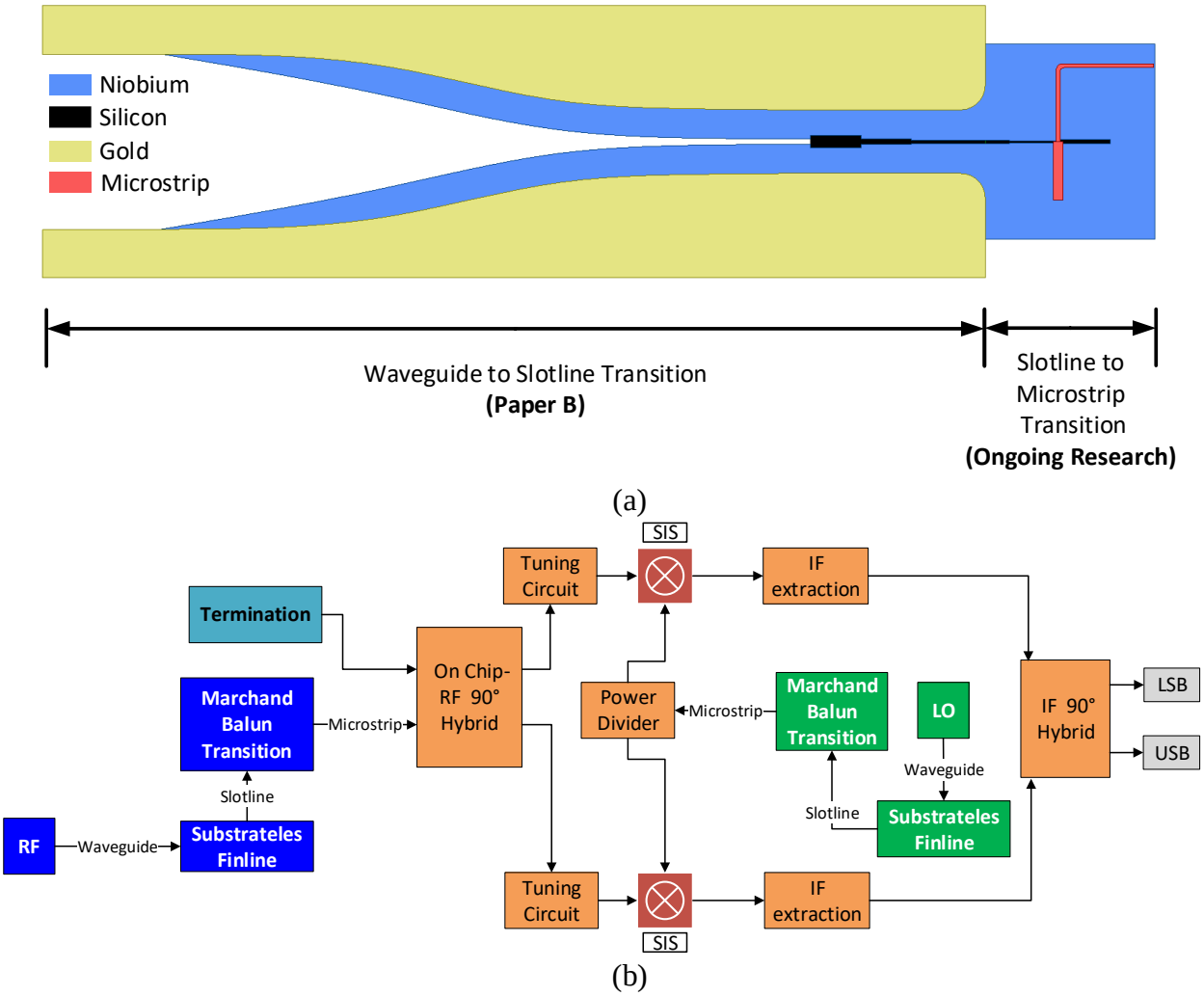

Figure. 6.1. *Future Outlook: Broadband mixer design. (a) Conceptual chip layout of waveguide to microstrip transition employing substrateless finlines developed in [Paper B] and the Marchand balun presented in Chapter 5. This transition could be used for RF and LO in a future SIS mixer design. (b) Conceptual block diagram for a sideband separating receiver employing the waveguide to microstrip transition shown in picture "a". The complete chip may include 2 waveguides to microstrip transition for LO and RF, on chip RF hybrid, on chip power divider for the LO signal and tuning circuitry for the SIS.*

Appendix I - Simplified equations for third-order Chebyshev Marchand balun calculation.

The following equations can be used for calculating a third-order Marchand Balun [56] and serve as a starting point for optimization:

$$z_3 = \sqrt{zos} \tag{I.1}$$

$$z2 = -\sqrt{zos} + (zos + \frac{\alpha^2 + \beta^2}{(\alpha - 1)\tan^2\theta})^{\frac{1}{2}} \tag{I.2}$$

$$z1 = \frac{\alpha^2 + \beta(\beta + z2\ \tan\theta)}{\alpha^2 + (\beta + z2\ \tan\theta)^2} z2\ tan^2\theta \tag{I.3}$$

$$\alpha = zos(\frac{1 + \tan^2\theta}{1 + zos\ tan^2\theta}) \tag{I.4}$$

$$\beta = \sqrt{zos}\,(1 - zos)\frac{\tan\theta}{1 + zos\ \tan^2\theta} \tag{I.5}$$

The terms α and β are used solely to simplify the presentation of the equations. Meanwhile, the variable θ , express in degrees, defines the theoretical bandwidth of the Chebyshev response. The relation between θ and the overall bandwidth of the transformer was numerically calculated in [56], showing an inverse nonlinear relation between these 2 variables. It is important to note that all the impedances have been normalized by ZoM in the equations.

Appendix II - Fabrication Process of Marchand Balun Test Chips

The process employed for fabricating the samples is detailed in Figure. II. The samples were fabricated from a silicon-on-insulator (SOI) substrate with a 300 µm handle layer, 2 µm barrier layer SiO2 and 30 µm device layer. The SOI structure facilitates handling the thin devices and provides a natural etch-stop layer for the Si etching.

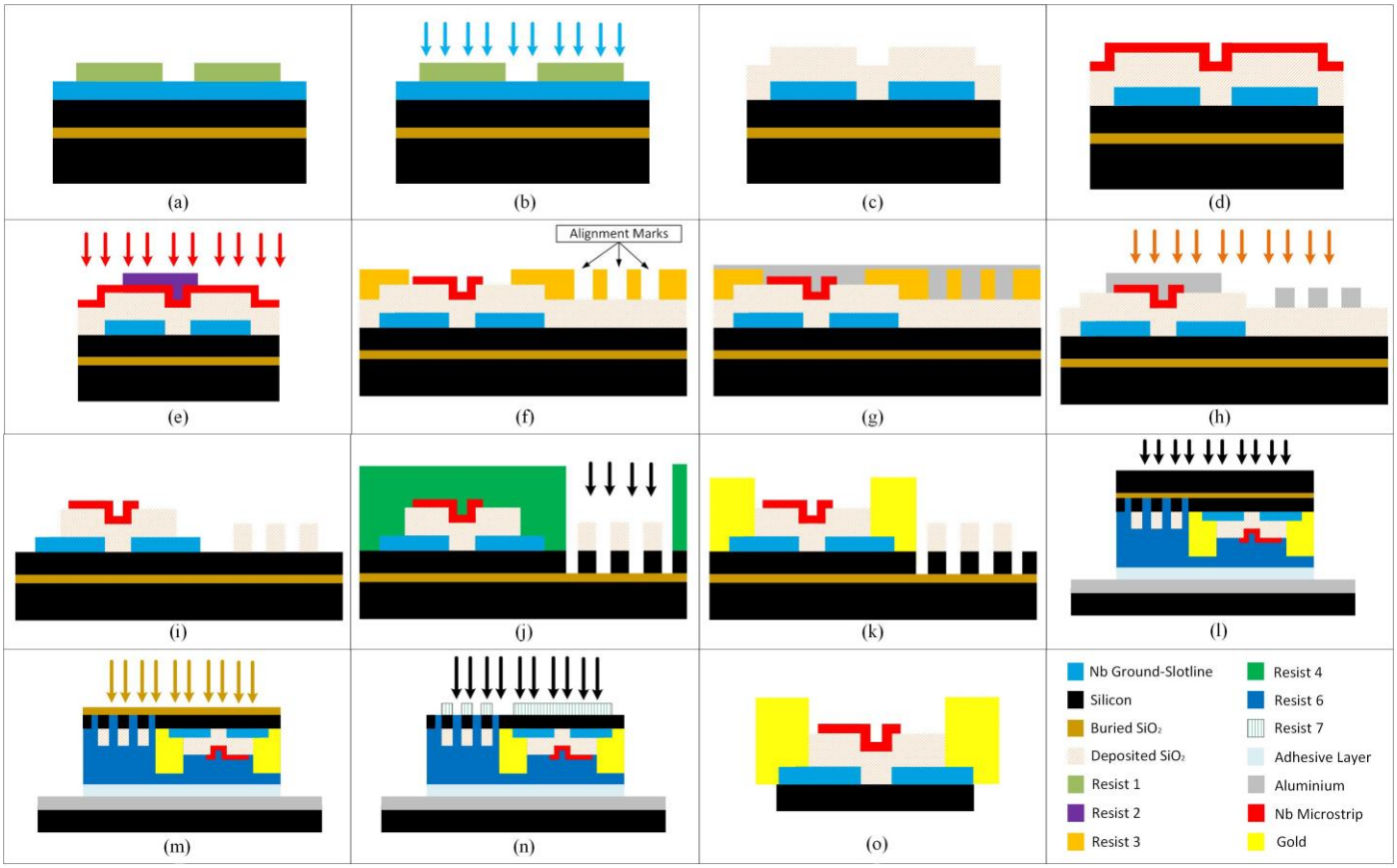

Figure II. *Simplified fabrication process. (a) First lithography over previously sputter Nb layer. (b) Dry etching of Nb layer for slotline definition. (c) Magnetron sputtering of SiO_2 layer. (d) Magnetron sputtering of second Nb layer. (e) Second lithography and dry etch of Nb layer for microstrip definition. (f) Third lithography. Note that certain alignment marks are patterned for transferring them into the SiO_2 layer. (g) Sputtering of 100 nm Al. (h) Lift off Al and dry etching of SiO_2 layer. (i) Strip of Al hard mask. (j) Fourth lithography and transferring of alignment marks into Si. (k) Electroplating of beamleads. (l) The sample is mounted for backside processing. Dry etch of handle layer. (m) Dry etching buried SiO_2. (n) Fifth lithography step and anisotropic etching of Si device layer. (o) Release of devices.*

After carefully cleaning the handle layer surface, a film of 450nm Nb layer is deposited by dc magnetron. Afterwards, the first lithography shown in Figure II.a creates a photoresist soft-mask over the Nb layer. This mask is later employed to define the slotline by dry etching the Nb layer in a reactive ion etching (RIE) process. Then, the 1.3 µm SiO_2 layer is deposit by a reactive RF magnetron sputtering. Furthermore, a second 450 nm Nb layer is deposited over the SiO_2 in the same vacuum run. The microstrip lines are created over this last Nb layer with a second lithography and dry-etching, as depicted in Figure II.e. This is followed by the third lithography shown in Figure II.f and the sputtering of a 100 nm Al layer, as illustrated by Figure II.g. The lift-off in acetone of the Al layer defines a hard mask for the SiO2 dry-etching process shown in Figure II.h. In addition, in this process stage, specially designed alignment marks are patterned in the SiO_2. This oxide layer will act as a hard mask for further transferring these alignment marks into the backside of the Si device layer with the help of a Bosh process. The deep Si etching by the Bosch process is depicted in Figure II.j. The Figure demonstrates how a thick photoresist allows the deep etching of the alignment marks but protects the rest of the sample. The alignment marks transfer will prove to be helpful in the last steps of the process since they will transform backside lithography into frontside lithography. This is advantageous since a better alignment could be easily obtained in frontside lithography.

After removing the thick photoresist, the beamleads are created through electroplating process, as depicted in Figure II.k. Afterwards, the chip is mounted upside down on a 4-inch Si carrier wafer for backside processing. The mounting process involves a release layer and an adhesive layer. The subsequent dry etch illustrated in Figure II.l and Figure II.m are employed to remove the handle layer and the buried oxide layer, respectively. The final lithography defines the chip shapes and uses the alignment marks patterned in the backside of the device layer. Therefore, a thick photoresist etch mask could be created on the backside. This soft-mask is used for the final anisotropic etching that complete the device definition. Finally, the devices are released when the adhesive and release layer are dissolved in a solvent.

Bibliography

[1] ROGALSKI, A.; SIZOV, F. Terahertz detectors and focal plane arrays. *Opto-electronics Review*, 2011, vol. 19, no 3, p. 346-404.

[2] PICKWELL, E.; WALLACE, V. P. Biomedical applications of terahertz technology. *Journal of Physics D: Applied Physics*, 2006, vol. 39, no 17, p. R301.

[3] FERGUSON, Bradley; ZHANG, Xi-Cheng. Materials for terahertz science and technology. *Nature materials*, 2002, vol. 1, no 1, p. 26-33.

[4] FARRAH, Duncan, et al. far-infrared instrumentation and technological development for the next decade. *Journal of Astronomical Telescopes, Instruments, and Systems*, 2019, vol. 5, no 2, p. 020901.

[5] SONG, Ho-Jin; NAGATSUMA, Tadao. Present and future of terahertz communications. *IEEE transactions on terahertz science and technology*, 2011, vol. 1, no 1, p. 256-263.

[6] BILLADE, Bhushan, et al. Performance of the first ALMA band 5 production cartridge. *IEEE Transactions on Terahertz Science and Technology*, 2012, vol. 2, no 2, p. 208-214.

[7] RASHID, Hawal, et al. Frequency multiplier based on distributed superconducting tunnel junctions: Theory, design, and characterization. *IEEE Transactions on Terahertz Science and Technology*, 2016, vol. 6, no 5, p. 724-736.

[8] KRAUSE, Sascha, et al. Noise and IF gain bandwidth of a balanced waveguide NbN/GaN hot electron bolometer mixer operating at 1.3 THz. *IEEE Transactions on Terahertz Science and Technology*, 2018, vol. 8, no 3, p. 365-371.

[9] ARMSTRONG, Carter M. The truth about terahertz. *IEEE Spectrum*, 2012, vol. 49, no 9, p. 36-41.

[10] COLLABORATION, Event Horizon Telescope, et al. First M87 event horizon telescope results. The shadow of the supermassive black hole. *Astrophys. J. Lett*, 2019, vol. 875, no 1, p. L1.

[11] "NOrthern Extended Millimeter Array NOEMA", IRAM Institut de Radioastronomie Millimétrique. [Online]. Available: https://www.iram-institute.org/EN/noema-project.php

[12] "Atacama Pathfinder Experiment APEX" [Online]. ESO, Max-Planck-Institut für Radiastonomie, Onsala Rymdobservatorium, Available: http://www.apex-telescope.org/ns/

[13] "Atacama Large Millimiter/submillimiter Array ALMA", ESO. [Online]. Available: https://www.almaobservatory.org/en/home/

[14] GREAVES, Jane S., et al. Phosphine gas in the cloud decks of Venus. *Nature Astronomy*, 2020, p. 1-10.

[15] MATSUSHITA, Yuko, et al. A very compact extremely high velocity flow toward MMS 5/OMC-3 revealed with ALMA. *The Astrophysical Journal*, 2019, vol. 871, no 2, p. 221.

[16] CARPENTER, John, et al. The ALMA Development Program: Roadmap to 2030. *arXiv preprint arXiv:2001.11076*, 2020.

[17] KRAUS, John D., et al. *Radio astronomy*. Powell, Ohio: Cygnus-Quasar Books, 1986.

[18] P.Y. Aghdam, "Characterization of the Specific Capacitance of Superconducting Tunnel Junctions", Chalmers University of Technology, Gothenburg, 2015.

[19] MORGAN, Matthew; WEINREB, Sander. *A monolithic HEMT diode balanced mixer for 100-140 GHz*. IEEE, 2001.

[20] KOOI, Jacob W., et al. Quantum Limited SIS Receiver Technology for the Detection of Water Isotopologue Emission from Comets. *IEEE Transactions on Terahertz Science and Technology*, 2020, vol. 10, no 6, p. 569-582.

[21] WILSON, Thomas L.; ROHLFS, Kristen; HÜTTEMEISTER, Susanne. *Tools of radio astronomy*. Berlin: Springer, 2009.

[22] BARYSHEV, A. M., et al. The ALMA Band 9 receiver - Design, construction, characterization, and first light. *Astronomy & Astrophysics*, 2015, vol. 577, p. A129.

[23] KERR, Anthony R., et al. Development of the ALMA band-3 and band-6 sideband-separating SIS mixers. *IEEE Transactions on Terahertz Science and Technology*, 2014, vol. 4, no 2, p. 201-212.

[24] YAGOUBOV, Pavel, et al. Wideband 67− 116 GHz receiver development for ALMA Band 2. *Astronomy & Astrophysics*, 2020, vol. 634, p. A46.

[25] DEAL, W. R., et al. InP HEMT integrated circuits operating above 1,000 GHz. *2016 IEEE International Electron Devices Meeting (IEDM)*. IEEE, 2016. p. 29.1. 1-29.1. 4.
[26] MOSCHETTI, Giuseppe, et al. A 183 GHz metamorphic HEMT low-noise amplifier with 3.5 dB noise figure. *IEEE Microwave and Wireless Components Letters*, 2015, vol. 25, no 9, p. 618-620.
[27] POZAR, David M. *Microwave engineering*. John Wiley & sons, 2011.
[28] HENKE, Doug; CLAUDE, Stéphane. Design of a 70–116 GHz W-band turnstile OMT. *2014 44th European Microwave Conference*. IEEE, 2014. p. 456-459.
[29] Belitsky, V., Lapkin, I., Fredrixon, M., Meledin, D., Sundin, E., Billade, B., ... & Koops, A. (2018). SEPIA–a new single pixel receiver at the APEX telescope. *Astronomy & Astrophysics*, *612*, A23.
[30] MARAL, Gerard; BOUSQUET, Michel; SUN, Zhili. *Satellite communications systems: systems, techniques and technology*. John Wiley & Sons, 2020.
[31] ZENG, Lingzhen, et al. A Compact Machinable 90° Waveguide Twist for Broadband Applications. *IEEE Transactions on Microwave Theory and Techniques*, 2020, vol. 68, no 7, p. 2515-2520.
[32] BARALIS, Massimo, et al. Full-wave design of broad-band compact waveguide step-twists. *IEEE microwave and wireless components letters*, 2005, vol. 15, no 2, p. 134-136.
[33] AL-TARIFI, Muhannad A.; FILIPOVIC, Dejan S. Design and fabrication of a full W-band multi-step waveguide 90° twist. *IEEE Microwave and Wireless Components Letters*, 2016, vol. 26, no 11, p. 903-905.
[34] RUIZ-CRUZ, Jorge A.; MONTEJO-GARAI, José R.; REBOLLAR, Jesús M. Multi-section bow-tie steps for full-band waveguide polarization rotation. *IEEE Microwave and Wireless components letters*, 2010, vol. 20, no 7, p. 375-377.
[35] KIRILENKO, Anatoliy A.; KULIK, Dmitriy Y.; RUD, Leonid A. Compact 90° Twist Formed by a Double-Corner-Cut Square Waveguide Section. *IEEE transactions on microwave theory and techniques*, 2008, vol. 56, no 7, p. 1633-1637.
[36] LENZING, H. F.; GANS, M. J. Machined waveguide twist. *IEEE transactions on microwave theory and techniques*, 1990, vol. 38, no 7, p. 942-944.
[37] ROSENBERG, Uwe; BORNEMANN, Jens; AMARI, Smain. A compact and broadband 90-degree waveguide twist transformer for integrated waveguide subsystems. 2001.
[38] ASAO, Hideki; HIRAIWA, Go; KATAYAMA, Akiko. A compact 90-degree twist using novel ridged waveguide for integrated waveguide subsystems. *2006 European Microwave Conference*. IEEE, 2006. p. 1185-1188.
[39] KIRILENKO, Anatoliy A., et al. Comparative analysis of novel compact and usual smooth 90-degree twists. *Proceedings of International Conference on Antenna Theory and Techniques*. 2009. p. 328-330.
[40] CHEN, Lihan, et al. A Micromachined Terahertz Waveguide 90° Twist. *IEEE microwave and wireless components letters*, 2011, vol. 21, no 5, p. 234-236.
[41] CHATTOPADHYAY, Goutam, et al. Submillimeter-Wave 90° Polarization Twists for Integrated Waveguide Circuits. *IEEE microwave and wireless components letters*, 2010, vol. 20, no 11, p. 592-594.
[42] WITHINGTON, S.; YASSIN, G. An investigation of the input impedance of a microstrip probe in waveguide. *Proc. of the 8th Int. Symp. on Space Terahertz Technology*. 1997.
[43] KOOI, J. W., et al. A full-height waveguide to thinfilm microstrip transition. *Ninth International Conference on Therahertz Electronics*. 2001. p. 15-16.
[44] RISACHER, Christophe, et al. A 275–370 GHz Receiver Employing Novel Probe Structure. *International journal of infrared and millimeter waves*, 2005, vol. 26, no 6, p. 867-879.
[45] BILLADE, Bhushan; PAVOLOTSKY, Alexey; BELITSKY, Victor. An SIS Mixer with 2hf/k DSB Noise Temperature at 163-211 GHz Band. *IEEE Transactions on Terahertz Science and Technology*, 2013, vol. 3, no 4, p. 416-421.
[46] LEONG, Kevin MKH, et al. A 340–380 GHz integrated CB-CPW-to-waveguide transition for sub-millimeter-wave MMIC packaging. *IEEE microwave and wireless components letters*, 2009, vol. 19, no 6, p. 413-415.
[47] TAN, Boon-Kok; WITHINGTON, Stafford; YASSIN, Ghassan. A compact microstrip-fed planar dual-dipole antenna for broadband applications. *IEEE Antennas and Wireless Propagation Letters*, 2015, vol. 15, p. 593-596.

[48] VASSILEV, V.; BELITSKY, Victor. Design of sideband separation SIS mixer for 3 mm band. *Proceedings of the Thirteenth International Symposium on Space Terahertz Technology*. 2001. p. 373-382.
[49] MEIER, Paul J. Two new integrated-circuit media with special advantages at millimeter wavelengths. *1972 IEEE GMTT International Microwave Symposium*. IEEE, 1972. p. 221-223.
[50] TAN, B.; YASSIN, Ghassan. Unilateral finline transition at THz frequencies. *Proceedings of the Twentieth International Symposium on Space Terahertz Technology*. 2009. p. 263-266.
[51] TAN, Boon-Kok, et al. A 650 GHz unilateral finline SIS mixer fed by a multiple flare-angle smooth-walled horn. *IEEE Transactions on Terahertz Science and Technology*, 2011, vol. 2, no 1, p. 40-49.
[52] CHANGFEI, Yao; JINPING, Xu; MO, Chen. Design of Ka-band antipodal finline mixer and detector. *Journal of Semiconductors*, 2009, vol. 30, no 5, p. 055009.
[53] CHATTOPADHYAY, Goutam; CARLSTROM, John E. Finline ortho-mode transducer for millimeter waves. *IEEE microwave and guided wave letters*, 1999, vol. 9, no 9, p. 339-341.
[54] YASSIN, Ghassan, et al. A 350-GHz SIS antipodal finline mixer. *IEEE Transactions on microwave theory and techniques*, 2000, vol. 48, no 4, p. 662-669.
[55] TAN, Boon Kok. *Development of coherent detector technologies for sub-millimetre wave astronomy observations*. Springer, 2015.
[56] TRIFUNOVIC, Velimir; JOKANOVIC, Branka. Review of printed Marchand and double Y baluns: Characteristics and application. *IEEE Transactions on Microwave Theory and Techniques*, 1994, vol. 42, no 8, p. 1454-1462.
[57] KONGPOP, U., et al. Slotline stepped circular rings for low-loss microstrip-to-slotline transitions. *IEEE microwave and wireless components letters*, 2007, vol. 17, no 2, p. 100-102.
[58] ZINIERIS, M. M.; SLOAN, R.; DAVIS, L. E. A broadband microstrip-to-slot-line transition. *Microwave and optical technology letters*, 1998, vol. 18, no 5, p. 339-342.
[59] SCHIEK, B.; KOHLER, J. An improved microstrip-to-microslot transition. *IEEE Transactions on Microwave Theory and Techniques*, 1976, vol. 24, no 4, p. 231-233.
[60] DING, Jiang-Qiao; ZHAO, Yun; SHI, Sheng-Cai. A full WR-3 band and low-loss 90° waveguide twist based on CNC. *IEEE Transactions on Terahertz Science and Technology*, 2019, vol. 10, no 1, p. 93-96.
[61] SCHIEBLICH, CHRISTIAN; PIOTROWSKI, J. K.; HINKEN, J. H. Synthesis of optimum finline tapers using dispersion formulas for arbitrary slot widths and locations. *IEEE transactions on microwave theory and techniques*, 1984, vol. 32, no 12, p. 1638-1645.
[62] NORTH, Chris; YASSIN, Ghassan; GRIMES, Paul. Rigorous analysis and design of finline tapers for high performance millimetre and submillimetre detectors. *Seventeenth International Symposium on Space Terahertz Technology*, 2006. p. 284-287.
[63] VALE, Christopher AW; MEYER, Petrie. Designing high-performance finline tapers with vector-based optimization. *IEEE Transactions on Microwave Theory and Techniques*, 1999, vol. 47, no 12, p. 2467-2472.
[64] "High Frequency Electromagnetic Simulation Software HFSS", Ansys. [Online]. Available: https://www.ansys.com/products/electronics/ansys-hfss
[65] ROZZI, Tullio, et al. Hybrid modes, substrate leakage, and losses of slotline at millimeter-wave frequencies. *IEEE transactions on microwave theory and techniques*, 1990, vol. 38, no 8, p. 1069-1078.
[66] EBNABBASI, Khabat, et al. Taper design of Vivaldi and coplanar tapered slot antenna (TSA) by Chebyshev transformer. *IEEE transactions on antennas and propagation*, 2012, vol. 60, no 5, p. 2252-2259.
[67] Kerr, A. R. Surface impedance of superconductors and normal conductors in EM simulators. *MMA Memo* 245, 1999, p. 1-17.
[68] BELITSKY, Victor, et al. Superconducting microstrip line models at millimeter and sub-millimeter waves and their comparison. *14th Space Terahertz Symposium*, 2003, p. 456-465.
[69] IMAMURA, Takeshi; SHIOTA, Tetsuyoshi; HASUO, Shinya. Fabrication of high quality Nb/AlO/sub x/-Al/Nb Josephson junctions. I. Sputtered Nb films for junction electrodes. *IEEE Transactions on applied superconductivity*, 1992, vol. 2, no 1, p. 1-14.
[70] "Virginia Diodes Incorporated VDI" [Online]. Available: https://www.vadiodes.com/en/
[71] RASHID, Hawal, et al. Superconducting 4–8-GHz hybrid assembly for 2SB cryogenic THz receivers. *IEEE Transactions on Terahertz Science and Technology*, 2014, vol. 4, no 2, p. 193-200.

[72] RISACHER, Christophe, et al. Waveguide-to-microstrip transition with integrated bias-T. *IEEE Microwave and Wireless Components Letters*, 2003, vol. 13, no 7, p. 262-264.
[73] RASHID, Hawal, et al. Frequency multiplier based on distributed superconducting tunnel junctions: Theory, design, and characterization. *IEEE Transactions on Terahertz Science and Technology*, 2016, vol. 6, no 5, p. 724-736.
[74] KOOI, J. W.; WALKER, C. K.; HESLER, J. A broad bandwidth suspended membrane waveguide to thin film microstrip transition. *9th Int. Conference on Teraherz Electronics, 15th-16th October*. 2001.
[75] TAN, Boon-Kok; YASSIN, Ghassan. A Slotline DC Block for Microwave, Millimeter, and Submillimeter Circuits. *IEEE Microwave and Wireless Components Letters*, 2019, vol. 29, no 9, p. 583-585.
[76] TUCKER, John R.; FELDMAN, Marc J. Quantum detection at millimeter wavelengths. *Reviews of Modern Physics*, 1985, vol. 57, no 4, p. 1055.
[77] NOVOSELOV, Evgenii; CHEREDNICHENKO, Sergey. Low noise terahertz MgB2 hot-electron bolometer mixers with an 11 GHz bandwidth. *Applied Physics Letters*, 2017, vol. 110, no 3, p. 032601.
[78] ASAYAMA, Shin'ichiro, et al. Development of ALMA Band 4 (125–163 GHz) receiver. *Publications of the Astronomical Society of Japan*, 2014, vol. 66, no 3.
[79] KOJIMA, Takafumi, et al. 275–500-GHz wideband waveguide SIS mixers. *IEEE Transactions on Terahertz Science and Technology*, 2018, vol. 8, no 6, p. 638-646.
[80] DURAN, Carlos, et al. 4GREAT-a four-color receiver for high-resolution airborne terahertz spectroscopy. *IEEE Transactions on Terahertz Science and Technology*, 2021, vol. 11, no. 2, pp. 194-204.
[81] VENTURI, Tiziana, et al. VLBI20-30: a scientific roadmap for the next decade. The future of the European VLBI Network. *preprint arXiv:2007.02347*, 2020.

Paper A

López, C., Desmaris, V., Meledin, D., Pavolotsky, A., & Belitsky, V. (2020).

Design and Implementation of a Compact 90° Waveguide Twist with Machining Tolerant Layout.

IEEE Microwave and Wireless Components Letters, *30*(8), 741-744.

Paper B

López, C., Desmaris, V., Meledin, D., Pavolotsky, A., & Belitsky, V. (2020).

Waveguide-to-Substrate Transition Based on Unilateral Substrateless Finline Structure: Design, Fabrication, and Characterization.

IEEE Transactions on Terahertz Science and Technology, *10*(6*), 668-676.*